Synthetic α-synuclein fibrils replicate in mice causing MSA neuropathology

Domenic Burger[1,2,*], Marianna Kashyrina[3,4,*], Lukas van den Heuvel[1,2,*], Hortense de La Seiglière[3], Amanda J. Lewis[1,2], Francesco De Nuccio[4], Inayathulla Mohammed[1,2,5], Jérémy Verchère[6], Cécile Feuillie[7], Mélanie Berbon[7], Marie-Laure Arotcarena[3], Aude Retailleau[3], Erwan Bezard[3], Marie-Hélène Canron[3], Wassilios G. Meissner[3,8], Antoine Loquet[7], Luc Bousset[9], Christel Poujol[10], K. Peter R. Nilsson[11], Florent Laferrière[3], Thierry Baron[6], Dario Domenico Lofrumento[12], Francesca De Giorgi[3], Henning Stahlberg[1,2,#] & François Ichas[3,12,#].

1. Laboratory of Biological Electron Microscopy, Institute of Physics, School of Basic Science, EPFL, Route de la Sorge, 1015 Lausanne, Switzerland
2. Department of Fundamental Microbiology, Faculty of Biology and Medicine, UNIL, Route de la Sorge, 1015 Lausanne, Switzerland
3. Univ. Bordeaux, CNRS, Institut des Maladies Neurodégénératives, UMR 5293, F-33000 Bordeaux, France
4. Univ. Salento, Department of Experimental Medicine, Human Anatomy, I-73100 Lecce, Italy
5. Dubochet Center for Imaging, Lausanne, Genopode (UNIL), EPFL, 1015 Lausanne, Switzerland
6. Univ. Lyon, ANSES, Neurodegenerative Diseases Unit, F-69364 Lyon, France
7. Univ. Bordeaux, CNRS, Bordeaux INP, CBMN, UMR 5248, F-33600 Pessac, France
8. CHU Bordeaux, Service de Neurologie des Maladies Neurodégénératives, IMNc, F-33000 Bordeaux, France
9. Univ. Paris-Saclay, CNRS, CEA, LMN, UMR 9199, F-92265 Fontenay-aux-Roses, France
10. Univ. Bordeaux, CNRS, INSERM, Bordeaux Imaging Center, UMS 3240, US 4, F-33000 Bordeaux, France
11. Department of Physics, Chemistry and Biology, Linköping University, Linköping, Sweden
12. Univ. Salento, Department of Biological and Environmental Sciences and Technologies, Human Anatomy, I-73100 Lecce, Italy

* Contributed equally

\# Correspondence to: henning.stahlberg@epfl.ch and francois.ichas@inserm.fr

Abstract

Multiple system atrophy (MSA) is a rapidly progressive neurodegenerative disease of unknown etiology, typically affecting individuals aged 50-60 and leading to patient death within a decade[1–3]. Characterized by the presence of glial cytoplasmic inclusions (GCIs) primarily composed of fibrillar alpha-synuclein (aSyn)[4–8], formation of MSA neuropathology presents similarities to prion propagation[9,10]. While previous investigations have scrutinized fibrils extracted from MSA brains[11], their possible "protein-only" replication was questioned[12] and their capacity to induce GCIs in animal models was not explored. Conversely, the synthetic fibril strain 1B[13,14] assembled from recombinant human aSyn self-replicates autonomously *in vitro* and induces GCIs in mice[15], suggesting relevance to MSA. Here we report the high-resolution structural analysis of 1B fibrils as well as of the fibrils extracted from 1B-injected diseased mice presenting GCIs ($1B^P$). We demonstrate *in vivo* that conformational templating drives the replication of a fibril strain, leading in this case to MSA inclusion pathology. In addition to the similarity of 1B and $1B^P$, both structures mimic the fold adopted by aSyn in one of the protofilaments of the fibrils extracted from MSA patients[11]. Finally, reinjection of diluted crude mouse brain homogenates containing $1B^P$ into the brain of new mice reproduces the experimental MSA neuropathology seen with the parent synthetic seed 1B. Our findings thus identify 1B as a synthetic pathogen capable of self-replication *in vivo*. We also highlight regions in the $1B/1B^P$ structure which seem distinctive for the buildup of a MSA inclusion pathology, providing insights for future therapeutic development.

Main

MSA is characterized by the rapid invasion of the brainstem, the cerebellum and/or the basal ganglia by intracellular inclusions filled with fibrillar aSyn[4–8]. These inclusions appear in neurons and in oligodendrocytes (OLs), particularly within the myelinated bundles of the white matter[16–18]. The latter inclusions are called GCIs and are specific to MSA. They are only observed rarely in other sporadic alpha-synucleinopathies[2,3]. The phenomenon of a "step-by-step" progression that characterizes brain invasion by GCIs, and the speed at which the GCIs induce the death of neurons in myelinated tracts[3], has led to the notion that MSA may obey a molecular mechanism analogous to that governing the intracerebral diffusion of pathogenic prions[9,10]. According to this hypothesis, the specific aSyn fibril strain found in GCIs plays a central role as both initiator and propagator of the pathology[9,10].

aSyn fibrils in GCIs were first observed *in situ*[4–8], and extracted and described using electron microscopy more than 25 years ago[19,20]. Such fibrils, extracted using the detergent sarkosyl, were characterized at high resolution by cryo-transmission electron microscopy (cryo-EM)[11], but to date, it has not been demonstrated that they can self-replicate like prions or induce the formation of GCIs in

animal models. The hypothesis was put forward[12] that unknown cofactors might be required for the replication of these extracted assemblies.

In parallel to the extractive approach by Schweighauser et al.[11], three synthetic aSyn fibril strains were obtained from recombinant aSyn, and these fibrils could self-replicate *in vitro* without the need for an external cofactor, and induce GCIs in mice. Chronologically, the first strain was a non-helical double-filament fibrillar assembly (ribbons) composed of monomers of human aSyn, which were capable of inducing GCIs, but only in rats overexpressing human aSyn concomitantly[21]. The second strain corresponded to mouse synthetic aSyn fibrils, which could induce the delayed appearance of GCIs in non-transgenic mice[22]. Finally, the third case concerned a fibril strain that some of us isolated and characterized (strain 1B), formed this time of human recombinant aSyn, and capable of causing the rapid appearance of GCIs in interfascicular OLs of wild-type mice[15]. Unlike for the aSyn fibrils extracted from MSA patients, no high-resolution atomic structure of these three types of synthetic aSyn fibrils had so far been available. This prevented the comparison of these fibrils with the atomic models obtained from patients to understand the structural bases of their capacity to induce GCIs.

We here report the structural characterization of aSyn fibrils of strain 1B at a resolution of 1.94 Å and compare them to the aSyn filaments extracted from the brains of 1B-injected diseased mice in which GCIs formed ($1B^P$, resolved at 3.8 Å). The striking structural similarity between 1B and $1B^P$ demonstrates that a conformational templating and replication process is indeed taking place *in vivo* and that it is responsible for fibril growth and inclusion pathology buildup. Further, the structural analogy of the 1B and $1B^P$ fold with the human MSA fold found in patient 5 of the seminal study of Goedert's group[11] suggests that a similar conformational replication process underlies MSA in humans.

Neuropathology seeded in vivo by the synthetic fibril strain 1B

1B fibrils present a typical rod-like compact appearance with a fibril width compatible with the intertwining of two protofilaments[14] and a left-handed helicoidal twist (**Extended data Fig. 1a)**. We observed in our founder experiments that 1B was capable of seeding a particularly strong aSyn pathology in neuronal cultures (see also **Extended data Fig. 1b**) and *in vivo* in mice[13,14]. In this early work, we found that the pathology induced by 1B at early time points was made of Lewy neurites, neuronal cytoplasmic inclusions (NCIs), and most strikingly, of neuronal intranuclear inclusions (NIIs)[13,14]. NIIs are distinctive for MSA compared to Parkinson's disease or dementia with Lewy bodies (DLB)[23,24], in which NIIs are absent. This very cytopathological feature led us to investigate the possibility that the synthetic 1B fibrils could represent an MSA-like fibril strain. Using a directed anatomical approach and later time points, we observed that 6 months after intracerebral inoculation, 1B was indeed capable of causing the appearance of GCIs in the anterior commissure (AC) of wild-type mice[15], *i.e.*, in a major myelinated tract containing densely packed rows of interfascicular OLs. The time course and the prominence of the GCI pathology seeded in this tract supported the notion that

like in MSA[24,25], the aSyn pathology seeded by 1B fibrils originated in neurons and was secondarily propagated to OLs[15].

After 24 months, a proper "invasion" of the posterior limb of the AC and of the bed nucleus of the *stria terminalis* (BNST) by GCIs could be observed (**Fig. 1a-e**), while Iba1-positive microglia did not particularly cluster around aSyn inclusion pathology (**Fig. 1c,d**). Confocal 3D volume reconstructions of affected OLs in the BNST showed the typical "flame-like" cytoplasmic distribution of phosphorylated aSyn (**Fig. 1e**). Global distribution of GCIs in full horizontal sections of mouse brain from animals sacrificed 1.5, 12, or 24 months after 1B fibril injection in their right caudate putamen (CP) showed generalized spread of GCIs (**Fig. 1f,** green markers). This was particularly prominent in the animal sacrificed at 24 months: in addition to the AC and to the BNST, GCIs were found bilaterally in deep cortical layers and the subcortical white matter, the CP, and unilaterally in the *globus pallidus* (GP) (injection side), the internal capsule (injection side), the entopeduncular nucleus (injection side), the *substantia nigra* (SN) *pars reticulata* (injection side), and the medullary reticular nucleus (contralateral side). A hovering section overview corresponding to **Fig. 1a-e** can be found in the **Supplementary information Movie-1**.

Depending on the neuroanatomical structure and the time point under consideration, the experimental GCIs of **Fig. 1f** coexisted with a variable load of surrounding neuronal somatic aSyn inclusions (NCIs and NIIs), which represent the forefront of the somatic aSyn pathology at earlier time points to progressively make way to a growing population of GCIs, as previously reported[15,22] (see also **Extended Data Fig. 2).** This is supportive of a neuronal to oligodendroglial inclusion transfer as in MSA[24,25].

Seeding of GCIs by 1B was neither dependent on the strain of the wild-type mice used to conduct the experiment nor on the intracerebral injection site. When C57BL/6 mice (instead of 129SV) were inoculated with 1B above their right SN, 17 months later, numerous aSyn inclusions could be observed on the right side (**Extended Data Fig. 3a, b)**. Incidentally, note the depletion of tyrosine hydroxylase-positive neurons also on the right side in the *pars compacta* of this animal (compare **Extended Data Fig. 3b and c**). Here also, the aSyn inclusions that formed included numerous GCIs as demonstrated by co-staining the OL nuclei with Sox10 (**Extended Data Fig. 3a, b, d, e**). They were particularly obvious at the boundary in between the *pars reticulata* and the *pars compacta* and were absent on the left side (**Extended Data Fig. 3a, c, d, f**). Iba1-positive microglial cells were also observed but without evident signs of clustering around aSyn inclusion pathology (**Extended Data Fig. 3d, e, f**).

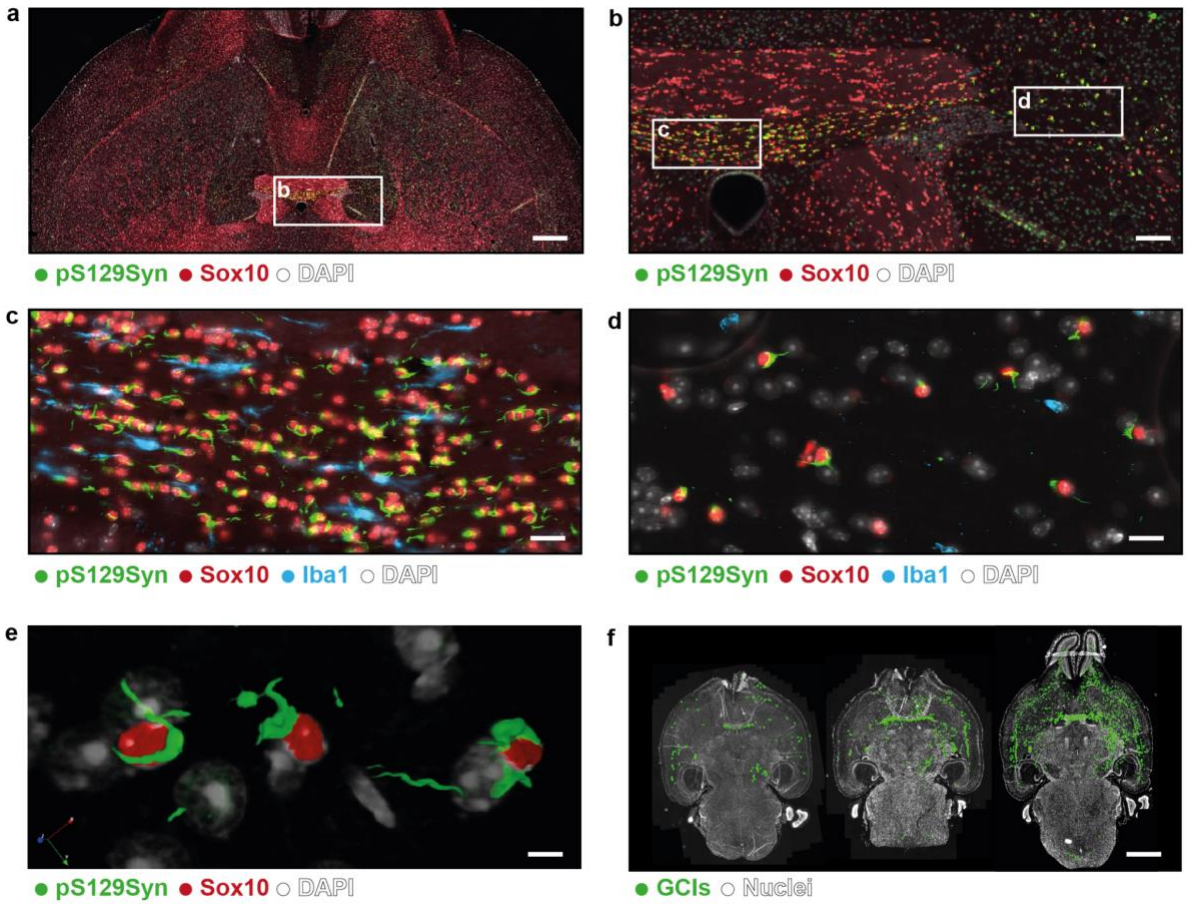

Fig. 1 | Seeding of GCIs in wild-type mice by alpha-synuclein fibrils of the 1B strain. **a.** Topographic immuno-fluorescence view of a horizontal brain section from a wild-type mouse injected 24 months earlier at the level of its right CP with 1B fibrils. aSyn inclusions are revealed using the anti-phospho aSyn antibody #64 (green), OLs by an antibody against the OL nuclear marker Sox10 (red), and nuclei using DAPI (white). The sectional plane intercepts horizontally the AC and the BNST (plain box) **b.** Higher magnification of the latter box evidencing the specific invasion by aSyn inclusions of the posterior limb of the AC (c), and of the BNST (d). **c.** Higher magnification showing that most of the interfascicular OLs populating the posterior limb of the AC bear aSyn inclusions, *i.e.*, GCIs, and sparse microglial cells are revealed using an antibody against Iba1 (blue). **d.** Higher magnification showing satellite Sox10-positive OLs populating the BNST that bear aSyn inclusions, *i.e.*, GCIs, and sparse Iba1-positive microglial cells are detectable. **e.** Bird's eye view of a confocal 3D volume reconstruction centered on 3 OLs of the BNST bearing GCIs, from the section shown in (a). See also **Supplementary information Movie-1**. **f.** Neuroanatomical distribution of GCIs in the brain of mice at 1.5 (left), 12 (center) and 24 months (right) post-1B injection in their right CP. Full brain horizontal sections. Every single GCI in (f) was manually annotated in the sections based on pS129Syn and Sox10. The 24-month section is the n+1 section adjacent to the one shown in (a). Scale bars: in a = 500 µm; in b = 100 µm; in c, d = 20 µm; in e = 5 µm; in f = 3 mm.

Tissue ultrastructure of the neuropathology induced by 1B

We analyzed the cellular inclusions in affected mouse brains (C57BL/6 mice), using CLEM with an adaptation of our previously described protocol[26,27]. Consecutive mouse brain tissue slices were imaged by fluorescence microscopy to identify the slices with pS129Syn-positive inclusions. These sections were then resin-embedded and heavy-metal stained in preparation for EM imaging. From the embedded sections, serial ultrathin sections were collected consecutively on glass slides and on EM grids, with the glass slides being used for immunohistochemistry (IHC) to re-localize the pS129Syn-positive cells and toluidine blue staining for optimal contrast of the sample. The resulting IHC and toluidine blue images were then successfully correlated to EM images taken on the consecutive grids. We used an animal of the 1B-injected series corresponding to **Extended Data Fig. 3a-f**. We imaged 30 pS129Syn-positive inclusions in a region straddling the right GP and CP and followed them throughout the brain tissue by serial sectioning. We could identify fibrillar material and membranous cytoplasmic sub-compartments in the pS129Syn-positive areas. For verification of the fibrillar morphology, we conducted room-temperature electron tomography on various positions within the IHC-positive regions of interest. Tomography data underscored the presence of fibrillar morphology in a dispersed, bundled, and clustered arrangement (**Fig. 2, Extended Data Fig. 4**). We additionally verified that the fibrillar material in the pS129Syn-positive IHC regions corresponded to aSyn protein assemblies, using immunogold labelling (**Extended Data Fig 5**).

The dispersed fibrillar material correlated with the pS129Syn-positive signal in the IHC image and could be found throughout all observed inclusions in the tissue. We measured the size of the nuclei of the cells bearing inclusions to be able to distinguish between NCIs and GCIs. Six cells with nuclei of more than 8.5 µm diameter were assumed to be neurons with NCIs, and sixteen pathological cells with a nucleus size below 8.5 µm were assumed to be GCIs in OLs. In many cases, the correlated area consisted of dispersed fibrillar material within a membranous local environment with various vesicular compartments. Fibril bundles could not be observed in all inclusions. If they were present, they varied strongly in length, thickness, curvature, and localization within the cell. Measurement of the identified bundles in 23 inclusions throughout 5 brain slices showed an averaged bundle length of 0.81 ± 0.41 µm. In most cases, the bundle length was of similar size of around 0.62 ± 0.07 µm. In a few exceptional cases, we measured bundles with individual lengths of 1.08 µm up to 3.64 µm (**Fig. 2a**). Fibrils appeared also in bigger clusters in irregular, chaotic arrangements, with fibrils radiating outward (**Fig. 2b**).

In addition, we could observe the regular proximity or direct contact of different and morphologically distinct cells to pathological ones (**Extended Data Fig. 6**). The morphology of these cells is reminiscent of cells described as “dark microglia” in mouse models for Alzheimer’s disease[28,29], as well as of cells recently described in human post-mortem MSA brain[30].

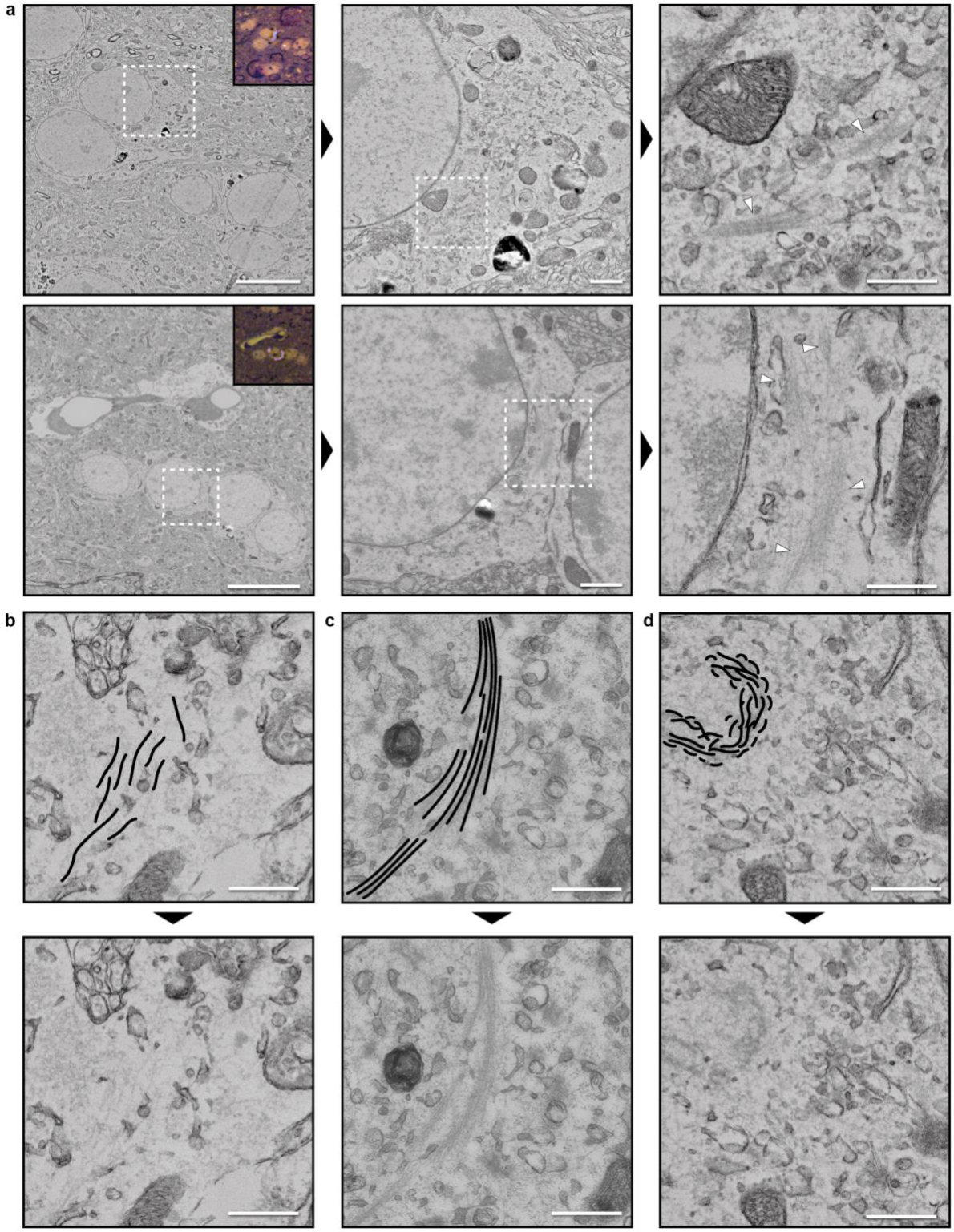

Fig. 2 | Tissue ultrastructure of 1B-seeded mouse brain. a. Correlative light and electron microscopy analysis of pS129Syn-positive regions. From left to right: overview EM image with insert of correlated LM data (scale bars = 10 µm); closer view at the pathological region at the indicated area (scale bars = 1 µm); and high magnification at settings taken for tomography to verify fibrillar material (scale bars = 500 nm). Fibril pathologies are indicated by white arrowheads. The LM inserts show the same location as in EM, with an overlay of IHC and toluidine blue staining and inverted color for better visualization. **b-d** High magnification EM images of different types of fibril arrangements, indicated by hand made drawings in the

upper row panels, and without indication in the lower row panels. **b:** "dispersed", **c:** "bundled", and **d:** "clustered" (scale bars = 500 nm).

To further challenge the pathogenic impact of 1B using a "humanized" *in vivo* model, we inoculated our 1B fibrils into hemizygous transgenic M83 mice expressing human A53T aSyn. These hemizygous mice have a normal lifespan and do not spontaneously develop fibrillar aSyn inclusions, despite the presence of one copy of the human aSyn A53T transgene[9,10]. We found that the intracerebral injection of 1B fibrils in these mice systematically caused their rapid demise in a notably synchronized fashion after only 16 weeks (**Fig. 3a**). Animals at death presented numerous intracerebral aSyn inclusions, in particular in the posterior limb of the AC, in which the presence of Lewy neurite bundles, GCIs and Glial Nuclear Inclusions (GNIs) could be observed (**Fig. 3b, c**). Non-seeded control M83 mice of similar age were healthy and showed no intracerebral aSyn inclusions (**Fig. 3b**). This indicated that like in the two previous wild-type mice strains, 1B fibrils were able to also cause the buildup of an inclusion pathology with cytopathological elements typical of MSA in transgenic mice expressing human A53T aSyn.

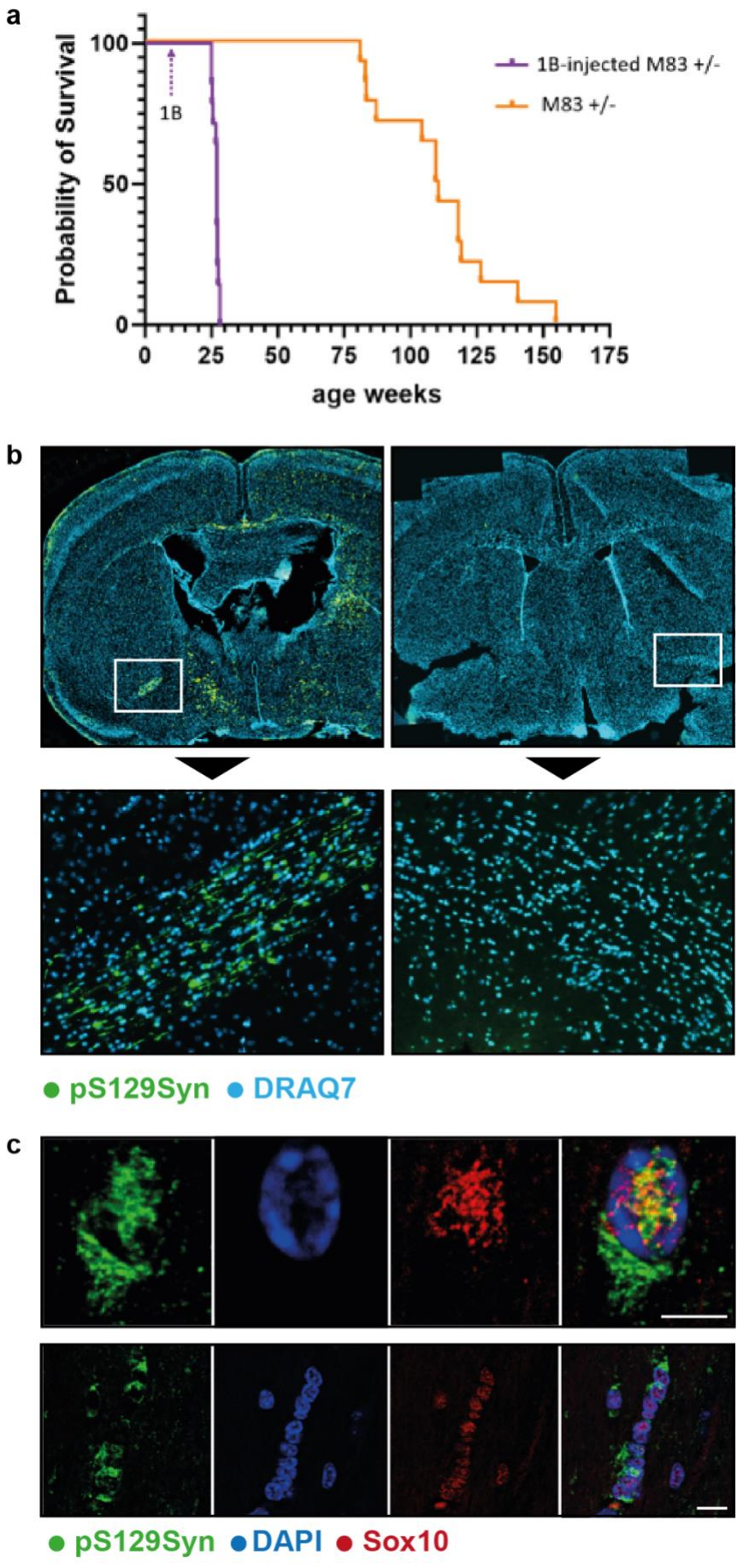
a
Probability of Survival
100
50
0
1B
1B-injected M83 +/-
M83 +/-
0
25
50
75
100
125
150
175
age weeks
b
pS129Syn
DRAQ7
c
pS129Syn
DAPI
Sox10

Fig. 3 | 1B is rapidly lethal to humanized M83 +/- mice in which it seeds GCIs and GNIs a. Kaplan-Meier survival curves of 28 hemizygous transgenic mice expressing human A53T aSyn (M83 +/-) without (14 mice, orange curve) of after (14 mice, purple curve) a unilateral injection (right CP) of 1B fibrils (time of injection: arrow). **b:** Illustrative concatenated immunofluorescence views of coronal brain sections of a 1B-injected M83 +/- mouse at the time of death (left), and of a M83 +/- mouse of similar age (right). White boxes: zoomed views centered on the posterior limbs of the AC. aSyn inclusions are revealed using the anti-phospho aSyn antibody EP1536Y (green), nuclei are revealed with DRAQ7 (blue). Note the numerous GCIs and LNs in the AC of the 1B-injected M83 +/- mouse (*nota bene*: the AC is a white matter tract that does not contain neuronal somata). Scale bars = 50 µm. **c:** 1B fibrils seed the buildup of aSyn GCIs and GNIs in oligodendrocytes (OLs) of 83+/- mice. Confocal imaging of a double immunofluorescence of aSyn inclusions (pS129aSyn) and of the OL-specific nuclear marker Sox10 in sections of the anterior commissure. At time of death (4 months post-injection) many commissural OLs harbor GCIs (lower image row). OLs containing both a GCI and a Glial Intranuclear Inclusion (GNII) can also be observed (upper image row). Scale bars = 5 µm.

Characterization of 1B and of its *in vivo* seeding product

Given the repeated capability of 1B to produce MSA inclusion pathology in different genetic mouse backgrounds, we thus embarked on the structure determination by cryo-EM of both 1B and of the fibrils populating the inclusion pathology seeded by 1B *in vivo*, here termed $1B^P$ to indicate the passage through the mouse brain.

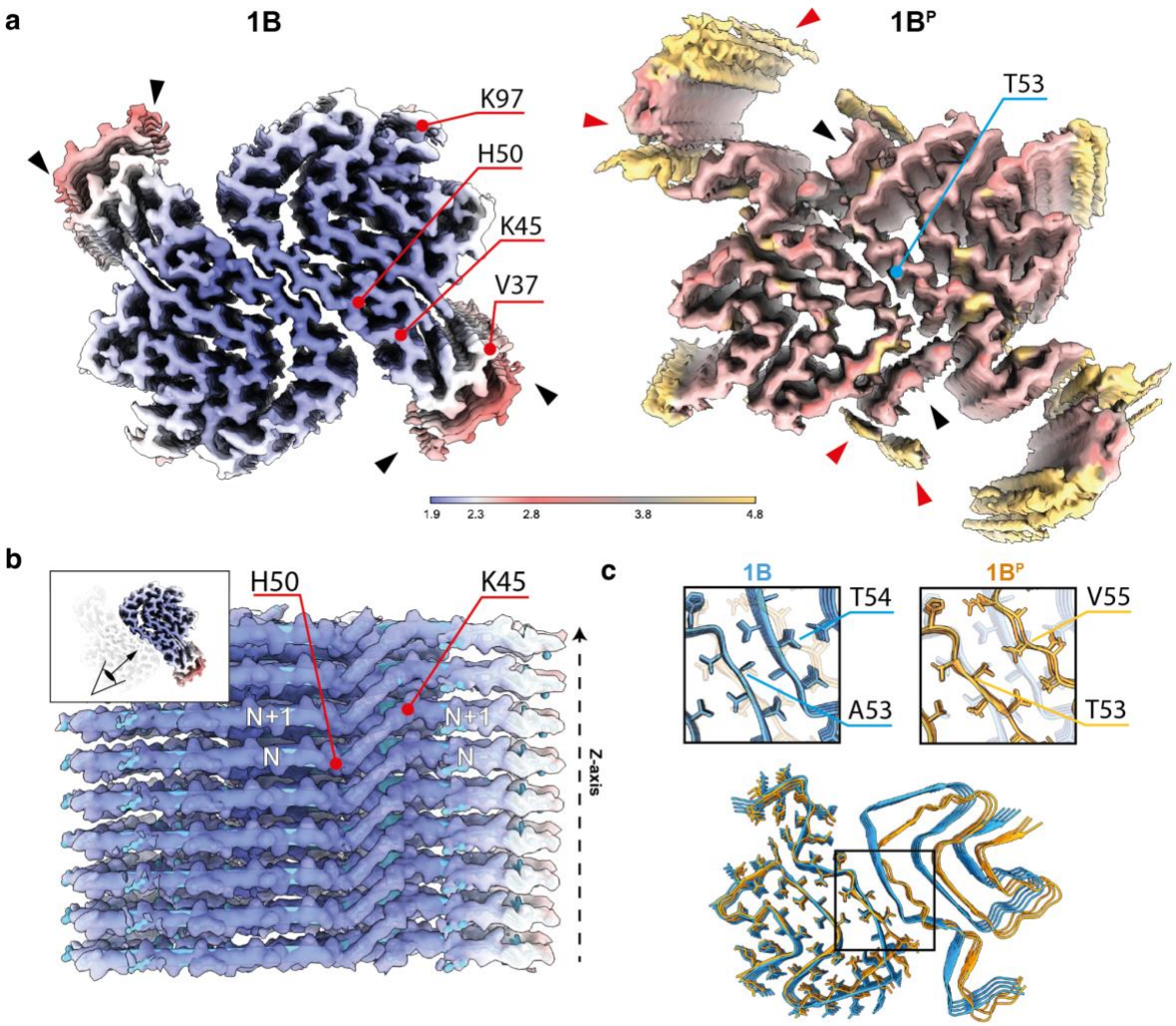

Fig. 4 | Structural organization of the 1B aSyn fibrils and of the 1B^P fibrils seeded by 1B *in vivo*. a. Density maps of 1B and 1B^P respectively, visualized with the local resolution range from 1.9 to 4.8Å. The model of 1B was built within the resolved densities starting from V37 to K97 (indicated). Wrapping around the stretch starting with V37, an additional density is present on both protofilaments, though at lower resolution (black arrow heads), which can also be observed at different positions in 1B^P. In addition, the structure of 1B^P indicates highly flexible areas that are poorly resolved at those densities and close to the N-terminal region (red arrow heads). **b.** Side view onto the protofilament interface (only one protofilament is shown), revealing the characteristic rise of the amyloid filament and the inter-rung connection at H50 to K47 of the next aSyn subunit (N and N+1). **c.** Sequence overlay of 1B (blue) and 1B^P (orange). One protofilament with stick representation, one with only the backbone. The overlay indicates slight alterations in the overall interface of the fibrils, with an RMSD of 1.433Å (compare to Table 1). Zoomed views of the protofilament interface highlight changes in interaction between side chains.

We first analyzed the 1B fibrils with cryo-EM and determined the structure at a resolution of 1.94Å (**Fig. 4a, Extended Data Fig. 7**). We found that they corresponded to the characteristic twisting of two identical amyloid protofilaments with a pseudo-Greek-key motif consisting of 9 beta-sheets. These lack C2 symmetry but are related by an approximate 2_1 screw symmetry. The map covers the sequence from G36 to K97, with an additional density attached alongside the starting sequence from G36 to V40 and

245 reaching toward the inside of the protofilament interface. As that density could not be unambiguously
246 assigned to any sidechains, we did not build an amino acid sequence for this stretch. Both identically
247 arranged protofilaments form their longest beta-sheet secondary structure from amino acids V52 to
248 K58. Along this stretch is the main protofilament-protofilament interaction, where the fibrils are held
249 together by electrostatic interactions with the opposite strand. The main electrostatic clusters are a
250 positive group formed by K43, K45, and H50, and a negative group formed by E57 and T59, flanking
251 the beta-sheet (**Extended Data Fig. 7c)**. Additionally, H50 appears to make an inter-rung connection
252 within the same protofilament to the following subunit along the Z-direction to K45 (**Fig 4b**). The
253 interaction between H50 and E57 causes the protofilaments to arrange in a half-step of the typical helical
254 rise, by binding the next aSyn subunit of the opposite strand at the 2.36Å and a resulting twist of 179.52
255 degrees.

256 To identify the conformation of aSyn fibrils in the seeded pathology we used the fibril purification
257 method previously developed for human MSA brain tissue[11]. The purification was successful in M83
258 +/- transgenic mice, diseased 16 weeks after inoculation with 1B. Despite the low yield of material after
259 the extraction procedure, pS129-aSyn positive fibrils were observed in negative stain imaging
260 (**Extended Data Fig. 8**). Subsequently, the sample was vitrified for structure determination with cryo-
261 EM.

262 The extracted material was heterogeneous, with limited concentration of suitable aSyn fibrils for
263 structure determination. We solved the structure of the extracted $1B^P$ fibrils out of 40 micrographs
264 (~0.1%) to a resolution of 3.8Å (**Fig. 4a**). The here termed $1B^P$ fibrils indicate the passage through the
265 mouse brain and are composed of two identical protofilaments, whose fold is highly similar to that of
266 the 1B fibrils seeding them (overall RMSD: 1.433Å), confirming a prion-like templated misfolding
267 mechanism that underlies inclusion formation in this mouse model. At the same time, an instance of
268 strain adaptation can be observed at the inter-protofilament interface, which spans from V52 to K58 in
269 1B but is shifted by one amino acid in $1B^P$ where it spans from G51 to E57. This shift, which we suppose
270 is driven by the A53T mutation expressed by M83+/– mice, brings side chains in the $1B^P$ steric zipper
271 that point towards each other into adjacent positions – as in the case of T53 and V55 (**Fig. 4c**) –
272 increasing the distance between Cα atoms in the backbone of the two protofilaments by more than 2Å
273 compared to 1B.

274 The fundamental organization of a single protofilament of 1B not only shows distinct similarities
275 to $1B^P$ but to already published structures as well, mainly the patient-purified MSA fibrils[11] (PDB:
276 6XYQ), the corresponding amplification[12] (PDB: 7NCK), the H50Q variant[31] (PDB: 6PEO), and wt-
277 and 1-121 aSyn variants[31,32] (PDB: 80QI and 6H6B) (**Fig. 5, Table 1**). The superimposition of these
278 structures to 1B highlights differences in the positioning of I88 and F94. The region, previously reported
279 as the C-pocket and acting as the binding site for ThT[33], is identical in arrangement for a subset of
280 structures and particularly in MSA fibrils (PDB: 6XYQ and PDB: 7NCK) and the H50Q variant (PDB:

6PEO). This is notable because like the 1B fibrils, also the H50Q fibrils (PDB: 6PEO) are ThT negative[31]. Consequently, the inaccessibility of the I88 pocket seems important to account for the ThT-negativity of 1B fibrils[13,14] (**Fig. 5a**).

In addition, the other ThT binding pocket located at the N-terminus (N-pocket)[33] of the fibrils also shows a modification compared to the structure of other ThT-positive fibrils. In the 1B structure, Y39 is shifted so that it faces T44 and E46. As a consequence, Y39 is not available for interaction with ThT in the N-pocket. Note that a similar conformation of the N-pocket with "shifted" Y39 presumably preventing ThT binding is also observed in the amplified MSA fibrils (PDB: 7NCK)[12] and the H50Q mutation (PDB: 6PEO), again in line with the parallel observation that seed amplification products templated on MSA brain extracts or on MSA cerebrospinal fluid are ThT-negative[34].

Collectively, these data support the hypothesis that closure of the ThT-binding pockets at the surface of the fibrils can explain the phenomenon of "ThT invisibility" and at the same time defines the pathophysiological specificity of 1B, $1B^P$ and MSA fibrils.

Besides regions involved in ThT binding, comparison with the other aSyn fibril folds also indicates the near identical arrangement of the H50Q variant to the 1B structure, with the exception of the H50 inter-rung side-chain orientation due to the point mutation. Whether this orientation is important and confers specific "MSA-like" properties to 1B is unknown, especially since the >3Å resolutions of PDB: 6XYQ and PDB: 7NCK do not allow conclusions on its existence in the MSA fibrils.

The 1B fibril structure also shows an outer, non-identified density stretch interacting with G36 to V40 (**Fig. 4a**), a feature which is also present in fibrils amplified from MSA (PDB: 7NCK), in H50Q fibrils (PDB:6PEO), and in $1B^P$ fibrils where poorly resolved densities flank the N terminal (**Fig. 4a**). This is remarkable, because these outer stretches block access of the disaggregase complex effector-component HSC70 to its binding site at the N-terminus of the fibrils, thus most probably preventing their disassembly and clearance[35]. This structural feature might thus represent a reason for the acute *in vivo* seeding capability of 1B[13].

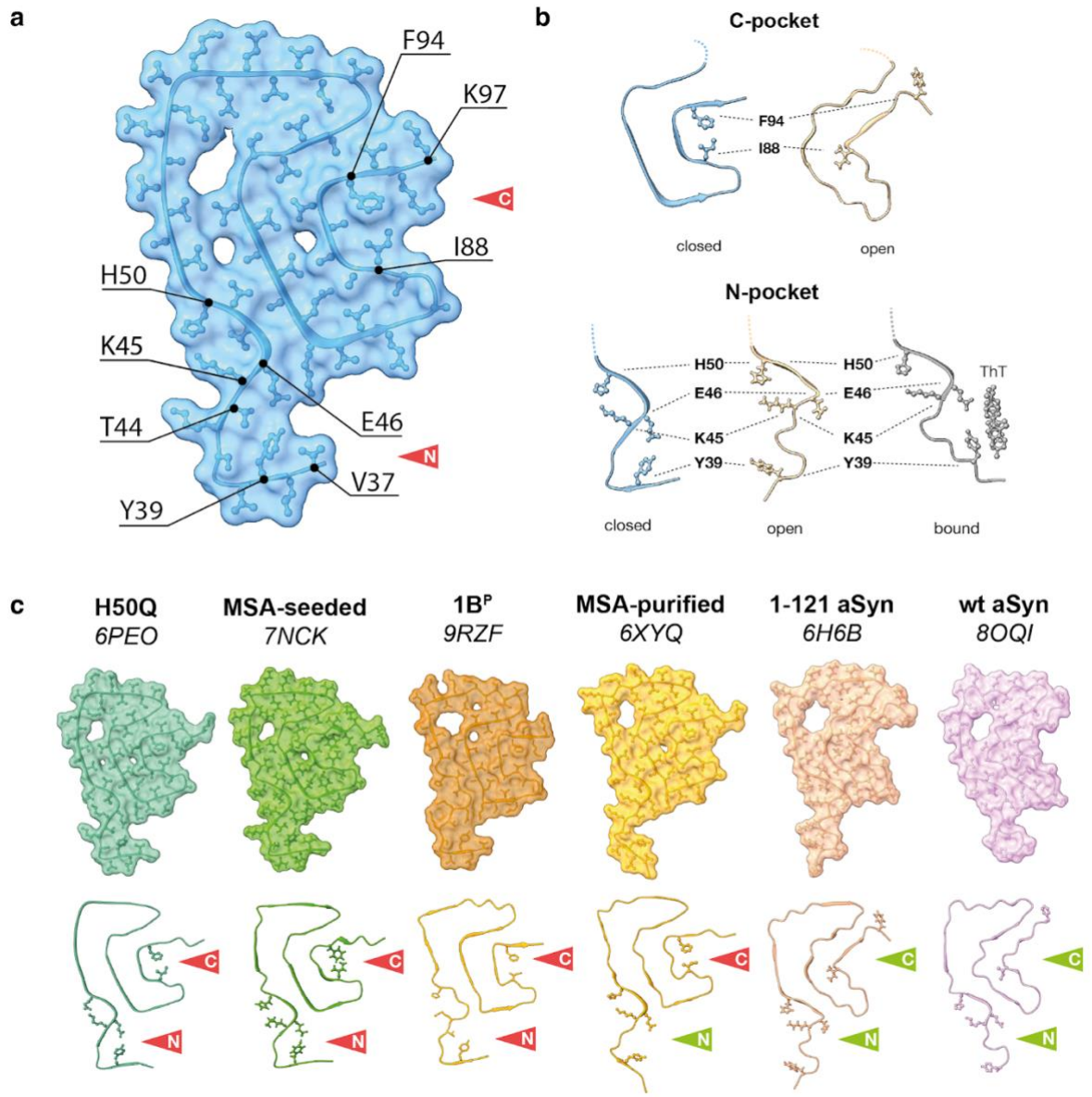

Fig. 5 | The C and N pockets are the best templated regions between 1B and 1B^{P}, are regions where ThT would have got bound (but here they are closed) and are the regions which are also closed in MSA and amplified MSA which is also ThtH negative. a. Conformation of one protofilament of 1B with surface volume representation. Structural comparisons of single protofilaments with similar fold are summarized with the respective RMSD values in Table 1. **b.** Zoomed view of the arrangement of the C-pocket on the example of 1B (left, PDB 9EUU) and 1-121 aSyn (right, PDB 6H6B) and the arrangement of the N-pocket on the example of 1B (left, PDB 9EUU), 1-121 aSyn (center, PDB 6H6B), and ThT-bound (grey) aSyn (right, PDB 7YNM). **c.** Shown are the full modelled sequences with transparent surface volume, as well as a ribbon representation with stick representation of Y39, K45, E46, H50, I88, and F94 for all compared structures. The open or closed state of either the C- or N-pocket are indicated by the green and red arrows respectively. Structural similarities are also given as RMSD values in Table 1.

In situ characterization of the neuropathology induced by 1B in wild type mice using h-FTAA

Despite repeated attempts, we were not able to recover enough fibrils from the brains of wild-type mice seeded with 1B to bring them to cryo-EM analysis, most likely because the inclusions are much less numerous than in 1B-injected M83+/- mice. We thus used the conformation-specific amyloid probe h-FTAA[36] to characterize the GCIs seeded by 1B directly in wild type mouse brain sections without extraction and to also compare them with the inclusions present in MSA (and DLB) post-mortem brain tissue sections. Indeed, and in agreement with previous work[37] we observed a clear cut difference between the signature of GCIs in MSA and that of Lewy bodies in DLB using fluorescence lifetime imaging microscopy (FLIM) of h-FTAA (**Extended Data Fig. 9**). Using this *in situ* approach we observed that the signature of the MSA inclusions was similar to that of the 1B brain inoculum in our mouse experiments and even closer to the signature of the inclusions seeded by 1B (**Extended Data Fig. 10, Table 3**). This was also in good agreement with the fact that the inclusion pathology seeded by 1B appeared positive to the MSA-specific silver impregnation staining technique of Gallyas[38] further suggestive of a structural analogy between 1B, 1B-seeded fibrils in wild type animals, and MSA fibrils in GCIs in human brain tissue sections (**Extended Data Fig. 11**). This is the same conclusion we drew from the cryo-EM structural comparisons of 1B with $1B^P$ and MSA fibrils which were extracted from brain tissue (**Fig. 5, Table 1**).

Brain homogenates containing 1BP can seed a MSA neuropathology in wild type mice

Finally, given the remarkable similarity between 1B, $1B^P$, and MSA filaments, we sought to determine whether $1B^P$, raised in transgenic animals, could still trigger MSA-like neuropathology in wild-type animals, as synthetic 1B does (**Fig. 6**). To address this question, we faced the challenge of the very low yield of the sarkosyl-based purification protocol for extracting $1B^P$ from 1B-seeded diseased mice, a yield insufficient to obtain the amount of intact fibrils required for in vivo reinoculation experiments. To overcome this limitation, we instead used a 10-fold dilution of a total brain homogenate from a 1B-seeded diseased mouse as the inoculum, without any purification step. We also focused on early post-injection effects (6 weeks) to maximize the likelihood of detecting a seeded synucleinopathy driven by trace amounts of 1BP fibrils delivered by the inoculum (*i.e.*, 2 µL of 10-fold diluted whole-brain homogenate). Our results indicate that $1B^P$ contained in the inoculate is capable of seeding anew an inclusion pathology in wild-type mice with the formation of NCIs, NIIs, GCIs and GNIs (**Fig. 4**) similar to what is observed when using synthetic 1B fibrils as seeds[13–15].

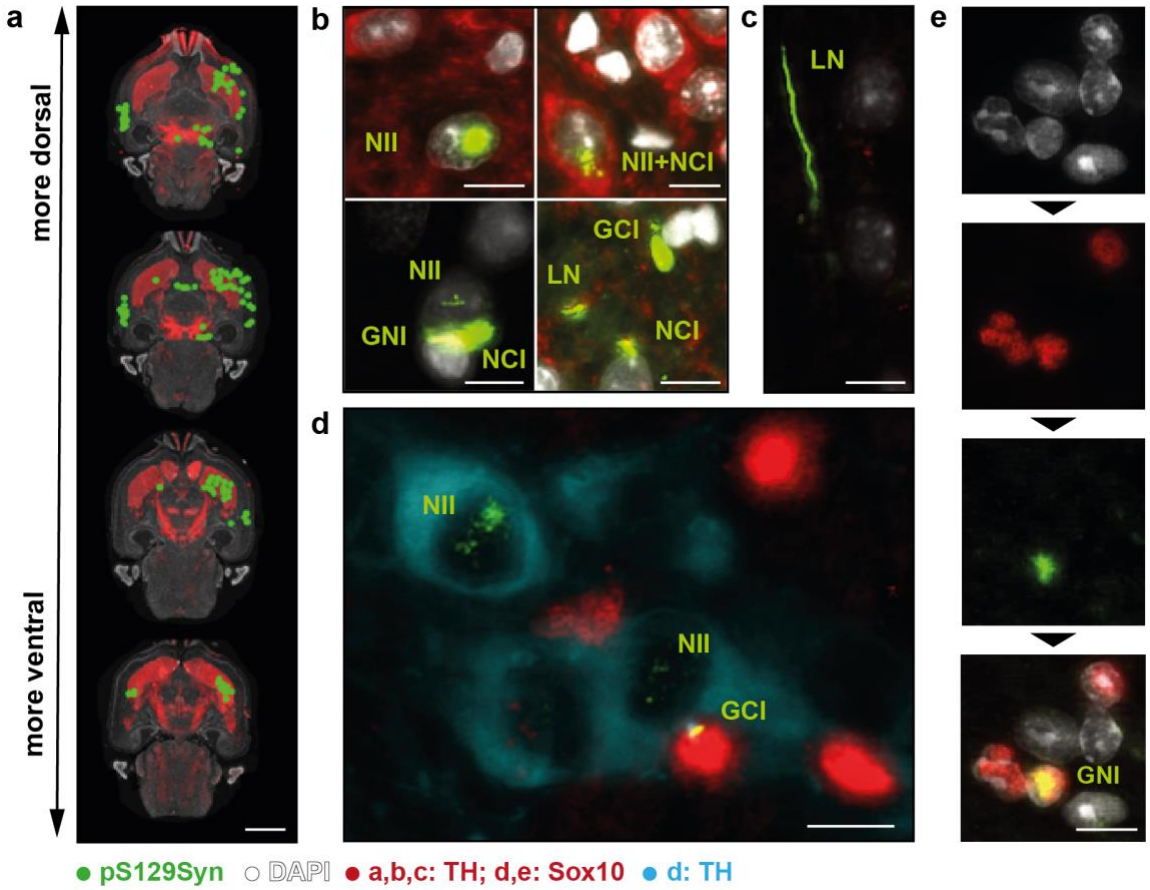

Fig. 6 | Early seeding of MSA pathology in wild type mice by brain homogenates containing 1B^{P} seeds. Diluted crude brain homogenates were prepared from prematurely dying M83+/- mice that had been injected 4 months earlier with 1B fibrils, brain homogenates were injected in the right CP of wild type 129SV mice. After 6 weeks, the wild-type mice were sacrificed, and their brains were processed for horizontal sectioning and immunofluorescence neuropathology. **a-c:** aSyn inclusions were revealed using an anti-phospho aSyn antibody (EP1536Y, green), the nigrostriatal tract was evidenced using an anti-Tyrosine Hydroxylase antibody (TH, red) and the nuclei were revealed with DAPI (white). **a:** 1 animal is displayed with 4 sections sampling the nigrostriatal tract along its dorso-ventral axis. Green dots are the annotations of the aSyn inclusions in the sections (Lewy neurites, NCIs, NIIs, GCIs and GNIs). **d,e:** Examples of MSA-specific aSyn inclusions seeded by the 1B^{P}-containing homogenate in sections stained for both TH (turquoise), the nuclear OL marker Sox10 (red), pS129Syn (#64, green), and the DNA intercalator DAPI (white). Fields of view in the right *Substantia Nigra*. **d**: 4 dopaminergic neurons (TH-positive cytoplasms) and 4 OLs (Sox 10-positive nuclei) can be seen (DAPI channel omitted for the sake of clarity). 3 aSyn inclusions can be observed in the same field which are pathognomonic of MSA: 2 neuronal intranuclear inclusions (NII); and 1 glial nuclear inclusion (GNI). **e**: Among 8 cells, a row of 4 OLs and a 5th solitary OL (Sox 10-positive nuclei) can be seen. One of the OLs harbors a nuclear inclusion (pS129Syn, GNI). As a control, diluted brain homogenates from spontaneously dying homozygous M83+/+ mice were also used as inoculate. While the brains of the latter mice contain aSyn inclusions, these are not of a MSA type, and their brain homogenates did not trigger any type of inclusion pathology in the recipient wild type mice (not shown). Scale bars = 3 mm (**a**) = 10 µm (**b-e**). 3D reconstructions and corresponding animated views of a selection of the inclusions shown here are presented in the **Supplementary information section: Movies 2 to 6.**

This indicates that the 1B strain characteristics are encoded in the pseudo-Greek-key motif of the 1B/1B^P fold rather than in the unattributable densities specifically observed in either 1B or in 1B^P after adaptation. It also indicates that the widening and the sliding of the protofilament interface acquired in 1B^P do not impinge on the MSA pathology-inducing characteristics of 1B/1B^P.

This is in line with the observation that the seeding of inclusions by 1B in cultured neurons is insensitive to mutations affecting residues located at the protofilament interface (H50Q, G51D, A53T and A53E) but that instead, it is abrogated by the mutation E46K which disrupts the E46-K80 salt bridge 'latch" necessary for the stabilization of the pseudo-Greek-key motif in the 1B fold (Extended data Fig. 12). Notably, the differential impact of the various aSyn mutations on the replication of 1B we report here is similar to what was reported for so-called MSA "prions" by Prusiner and his group[39,40].

In conclusion, the unattributed densities in 1B and 1BP, as well as the interface adaptations observed in 1BP, do not appear to play a significant role in the pathogenic activity of 1B/1BP. In other words, the fold kernel shared by 1B, 1BP, and MSA filaments is likely necessary and sufficient to induce MSA-like neuropathology.

Within this fold kernel, the regions of 1B which are templated with the highest fidelity in 1BP correspond to the closed N- and C- pockets (Extended Data Table 1). As previously discussed, such closure accounts for the ThT-invisibility of both 1B[13,14] and the amplified MSA filaments[34]. This is particularly relevant given that ThT-invisibility is also observed in two other synthetic fibril assemblies of unknown structure, both of which were reported to seed GCIs in vivo[21,22,41].

It is thus tempting to speculate that closed N- and C- pockets are also present in these latter fibrils, further supporting the idea that, within the fold kernel shared by 1B, 1B^P, and MSA filaments, the closure of the N- and C- pockets represents the minimal common structural determinant responsible for MSA pathology induction.

Discussion

We presented here the high-resolution structure of aSyn fibrils 1B as well as of their *in vivo* seeding product $1B^P$. Indicative of a high-fidelity conformational replication process, the structures present a remarkable similarity and are capable of perpetuating MSA pathology through passage in humanized and wild-type mice.

Notably, this study provides clear evidence of a protein-only replication process occurring *in vivo* and evidenced at a 3.8Å resolution. The templating fidelity of the synthetic 1B seeds, both *in-vitro* and in the mouse brain, is remarkable given the difficulty to efficiently amplify MSA brain extracts with structural preservation[12]. While we cannot rule out the presence of additional fibril polymorphs different from $1B^P$ in the 1B-inoculated mouse model, which may have arisen through secondary nucleation and are undetectable by cryo-EM, the robust propagation of the 1B protofilament fold provides strong support for a prion-like templating mechanism.

This notion is strengthened by our observation that brain homogenates containing $1B^P$ can trigger in wild-type mice the same MSA inclusion pathology as the one seen after 1B injection, indicating that untemplated secondary nucleations, if any, do not significantly participate in the MSA pathology seeded by 1B. Instead, the kernel common to $1B/1B^P$ defines - through a templated replication - the MSA strain characteristics of the fibrils (MSA kernel). Importantly, this MSA kernel is shared in one of the two protofilaments of MSA fibrils extracted from patient 5 in the seminal study of Schweighauser and colleagues[11], as well as the MSA fibrils resulting from the *in vitro* amplification of the same patient's sample[12].

Interestingly, the templating fidelity of the MSA kernel between 1B and $1B^P$ is most pronounced in two particular regions: the N- and C- pockets. These 2 regions are of particular interest because they define the binding sites for the amyloid probe ThT[33], but are closed and not accessible to the dye in the MSA kernel. Our data suggest that structural features of aSyn fibrils – specifically closed N- and C-pockets – are related to their ThT invisibility and their seeding properties, in particular their ability to seed GCIs. This is in agreement with the fact that the 3 synthetic fibril assemblies that have been reported to induce GCIs in mice and rats are all weak ThT binders, and that the fibrils amplified from MSA patient brain samples and CSFs[34] are ThT negative as well.

This collectively points to a major pathophysiological role of C- and N- pocket closure with direct relevance to MSA.

In the MSA kernel, the specific binding site around the C-pocket of I88 is closed by forming a "lever" with F94, mainly caused by the outward orientation of I88. Compared to other aSyn fibril structures with an open C pocket, in $1B/1B^P$, the inner "hook" of the pseudo-Greek-key motif along the stretches of V74 to F94 is shifted by one amino acid position starting at A85. As a result, A85 points

433 outwards at the most prominent position of the inner hook, which causes a consequential inversion of
434 sidechain positioning for the remaining sequence. In 1B/1B^P, this causes S87, a known modification
435 site for fibril inhibition by O-Glc-N acylation[42] or by phosphorylation[43] to be inaccessible, and I88 to
436 be positioned outwards, undergoing a connection with F94 and therefore closing the C-pocket.

437 Enforcing the post-translational modification of S87 or "forcing open" the C-pocket using small
438 molecules might thus represent promising means to derail the templating process during fibril growth,
439 and force fibril elongation to take place on a modified template which has lost part of the MSA kernel.
440 This would presumably not prevent fibril growth but could perhaps impinge on the acute replicative
441 and toxic properties of MSA fibrils and slow down disease progression.

442 The closed N-pocket is a shared characteristic of the 1B and 1B^P structures, and this was also
443 observed in the amplified MSA filaments from patient 5 [12]. However, fibrils extracted from MSA
444 patients [11] did not share the closed N-pocket conformation (**Fig. 5, Table 1**). Whether this points to a
445 dispensable pathogenic role of N- pocket closure remains to be determined.

446 Finally, it is worth noting that the ability of crude brain homogenates from MSA patients to seed
447 pathological inclusions in wild-type mice has – to our knowledge – not been reported to date. This may
448 be due to a lack of systematic investigation, but alternatively, it may suggest that the fibrils present in
449 human MSA brain samples are intrinsically less aggressive than 1B or 1B^P fibrils. If so, the higher
450 infectivity of the 1B/1B^P strain could result from the specific structural features not shared with patient-
451 derived fibrils. Notably, these include: (i) a closed versus open N-pocket; (ii) the pseudo-symmetric
452 arrangement of two identical protofilaments in 1B/1B^P, as opposed to the asymmetric fold of two
453 distinct protofilaments in MSA fibrils; and (iii) additional, unattributed densities in 1B and 1B^P, which,
454 although distinct, may obscure chaperone clearance sites in both. The relevance of these structural
455 differences remains to be determined. Regardless of the precise mechanism underlying the high seeding
456 efficiency, it is important to emphasize that, in the absence of prior structural knowledge of synthetic
457 or patient-derived α-synuclein fibrils, such materials should be handled with extreme caution and
458 appropriate personal protective measures.

459 Taken together, this study demonstrates the existence of a synthetic aSyn fibril strain that is capable
460 of inducing MSA-like pathology in WT mice and replicates in M83+/- mice through a protein-only
461 templating process. The high resolution achieved on the fibril seeds and the ultrastructural and structural
462 study of fibrils formed *in vivo* highlight the similarity of 1B and MSA fibrils, and postulate a link
463 between fibrillar structure, assembly, mechanism of prion-like seeding and spreading, as well as animal-
464 to-animal transmission.

465

Online methods

aSyn expression

Escherichia coli strain BL21(DE3) was transformed with pT7-7 aSyn wt vector[43] from Addgene, deposited by Hilal Lashuel (Addgene plasmid #36046; http://n2t.net/addgene:36046; RRID: Addgene_36046) and plated onto a Luria broth (LB) agar plate containing ampicillin (100 µg/mL) and 1 g/L glucose. A preculture in 5 mL of LB medium was inoculated with one clone and incubated at 37°C under 200 rpm shaking for 4 h. Cells from the LB preculture were recovered by centrifugation (1000× g, 10 min) and used for inoculating 200 mL of LB medium. Cells were grown overnight at 37°C under 200 rpm shaking and then diluted in 2 L of culture. Protein expression was induced by adding 0.5 mM isopropyl-β-d-thiogalactopyranoside during the exponential phase, evaluated at an optical density at 600 nm reaching 0.6. Cells were harvested after 5 h of culture at 30°C by a 7000× g centrifugation at 4°C, 20 minutes (JLA 8.1000, Beckman Coulter, Villepinte, France), and pellet was kept at −20 °C until purification.

aSyn purification

The pellets were resuspended in lysis buffer (10 mM Tris and 1 mM EDTA (pH 7.2) with protease inhibitor tablets (cOmplete, EDTA-free protease inhibitor cocktail, Roche, Basel, Switzerland) and sonicated at 50% max energy, 30 s on and 30 s off for three rounds with a probe sonicator (Q-Sonica, Newtown, CT, USA). The sonicated pellets were centrifuged at 20,000× g for 30 min, and the supernatant was saved. The pH of the supernatant was then reduced to pH 3.5 using HCl, and the mixture stirred at room temperature (RT) for 20 min and then centrifuged at 60,000× g for 30 min. The pellets were discarded. The pH of the supernatant was then increased to pH 7.4 with NaOH and then dialyzed against 20 mM tris-HCl (pH 7.4) and 100 mM NaCl buffer before loading onto a 75 pg HiLoad 26/600 Superdex column equilibrated with the same buffer with ÄKTA pure system. Monomeric fractions were collected and concentrated if needed by using Vivaspin 15R 2 kDa cutoff concentrator (Sartorius Stedim, Göttingen, Germany). Purification fractions were analyzed by polyacrylamide gel electrophoresis (PAGE) tris-tricine 13% dying with ProBlue Safe Stain. Protein concentration was evaluated spectrophotometrically by using absorbance at 280 nm and an extinction coefficient of 5960 M^{-1} cm^{-1}. Quantification of the preparations with a Pierce chromogenic LAL kit indicated a low endotoxin [lipopolysaccharide (LPS)] residual value of 0.03 to 0.06 EU per µg of recombinant protein.

aSyn fibrillization

Solutions of monomeric aSyn at 4 to 5 mg/mL in saline (H2O, 100 mM NaCl, and 20 mM tris-HCl pH 7.40) were sterilized by filtration through 0.22 µm Millipore single-use filters and stored in sterile 15 mL conical falcon tubes at 4°C. Sterilized stock was then distributed into safe-lock Biopur individually sterile-packaged 1.5 mL Eppendorf tubes as 500 µL aliquots and were seeded with 1% of 1B strain fibrils[13–15]. The tubes were cap-locked and additionally sealed with parafilm. All previous

steps were performed aseptically in a particle-free environment under a microbiological safety laminar flow hood. The samples were loaded in a ThermoMixer (Eppendorf, Hamburg, Germany) in a 24-position 1.5 mL Eppendorf tube holder equipped with a heating lid. The temperature was set to 37 °C, and continuous shaking at 2000 rpm proceeded for 4 days. 1B templating of the fibrillization products was quality-checked using the fibrilloscope[13–15].

Sonication

Prior to intracerebral injections, 1B aSyn fibril stocks (4 mg/mL) were distributed in cap-locked, sterile 0.5 mL polymerase chain reaction (PCR) tubes (Thermo Fisher Scientific, Bordeaux, France). Sonication was performed at 25 °C in a Bioruptor Plus water bath sonicator (Diagenode, Liège, Belgium) equipped with thermostatic control and automated tube carousel rotator. The sonication power was set to "high", and 10 cycles of 30 s on followed by 10 s off were applied. In agreement with our previous quantifications[13], over 80% of the fibrils were 50 nm-long or less after application of this protocol (not shown).

In vivo aSyn pathology

Adult 129SV (intrastriatal injections), C57BL/6 (nigral injections), and transgenic M83 (hemizygous, intrastriatal injections) were housed in a temperature-controlled (22 °C) and light-controlled environment on a 12 h light/12 h dark cycle with access to food and water ad libitum. The study design was approved by the French Ministry of Research and all experimental procedures were conducted in accordance with the European Communities Council Directive (2010/63/EU) for care of laboratory animals. The mice (6–8 weeks old) unilaterally received 2 µL of sonicated aSyn fibrils 1B (4 mg/mL) by stereotactic delivery at a flow rate of 0.4 µL/min, and the pipette was left in place for 5 min after injection to avoid leakage. Delivery was performed within the right striatum (coordinates from bregma: AP, −0.1; L, +2.5; DV, +3.8), or above the right substantia nigra (coordinates from bregma: AP, −2.9; L, −1.3; DV, −4.5). Wild-type mice (n=20) and transgenic M83 hemizygous mice (n = 28) injected with either PBS, 1B fibrils, or brain homogenates were euthanized after 6 weeks, 17 months, 24 months, or when reaching the humane endpoints defined as death regarding the transgenic M83 mice, and were transcardially perfused with either tris-buffered saline (pH = 7.4) followed by 4% paraformaldehyde in PBS pH = 7.4 at 4 °C, or with cacodylate buffer 0.1 M with 1 mM CaCl2 (pH = 7.4) followed by 4% paraformaldehyde plus 0.1% glutaraldehyde in 0.1 M cacodylate buffer (pH = 7.4). Brains were subsequently postfixed in the same fixative. For standard neuropathology, the brains were paraffin embedded, and 10 µm sections were cut with a rotative microtome (Leica, Milan, Italy). The sections of interest were deparaffinized and processed for epitope retrieval: the slides were immersed in citrate buffer pH 6 (Dako Agilent Technologies, Les Ulis, France) and placed in a pressure cooker (Bio SB, Santa Barbara, CA, USA) at 114°C-121°C for 10 min. After a cooling period of 20 min, the slides were washed twice for 5 min in PBS at room temperature. They were then processed for simple or double immunofluorescence using the following primary antibodies diluted at 1/500, or their

537 combinations: EP1536Y (Abcam) or pSyn#64 (Wako) for detecting phospho-S129–positive aSyn
538 inclusions; LB509 for detecting human aSyn (Abcam, mouse monoclonal); anti-Sox10 (Abcam, rabbit
539 monoclonal) for detecting OL nuclei; EP1532Y and anti-TH raised in chicken (anti-Tyrosine
540 Hydroxylase, Abcam) for detecting the nigrostriatal tract; and anti-Iba1 (Abcam) for detecting
541 microglia. DRAQ7 or DAPI were used to image the nuclei. The AlexaFluor-coupled secondary
542 antibodies were from Thermo Fisher (Alexa 488, 568, and 674). The sections were acquired using a
543 Pannoramic slide scanner (3D HISTECH, MM France) in epifluorescence mode, and multichannel
544 fluorescence optical sections of the samples were performed (thickness < 0.8 µm) using either a Zeiss
545 CD7 platform of a Leica SP5 Laser Scanning Confocal Microscope equipped with a spectral detector,
546 488, 561, and 633 nm laser lines, a motorized X-Y stage, and a mixed stepping motor/piezo Z controller.
547 The objective was 40×, and Z step size was set to 0.5 µm to produce stacks of 15 to 20 Z planes. The
548 pinhole was set to 1 airy unit. For 3D reconstructions and volume rendering/animations (corresponding
549 to 360° tilt series of composite max pixel projections images), raw 3-channel Z-stack images were
550 processed offline using Icy[44].

551 High content analysis (HCA) of 1B-seeded aSyn inclusions in primary neuronal 552 cultures expressing human aSyn and its variants

553 Timed inbred-pregnant C57BL/6JOlaHsd (aSyn KO) female mice were received from Envigo
554 (Puteaux, France) 2 days before initiation of the primary culture. The pregnant mouse was euthanized
555 by cervical dislocation, and the aSyn KO embryos (embryonic day 18) were surgically extracted and
556 cold-euthanized. Cortices were harvested from 8 of them, pooled, and dissociated enzymatically and
557 mechanically (using a neural tissue dissociation kit, C Tubes, and an Octo Dissociator with heaters;
558 Miltenyi Biotech, Germany) to yield a homogenous cell suspension pool of 8 individuals. The cells
559 were then plated at 20,000 per well in 96-well plates (Corning, BioCoat poly-d-lysine imaging plates)
560 in neuronal medium (MACS Neuro Medium, Miltenyi Biotech, Germany) containing 0.5% penicillin-
561 streptomycin, 0.5 mM alanyl-glutamine, and 2% NeuroBrew supplement (Miltenyi Biotech, Germany).
562 The cultures were maintained with 5% CO2 at 37°C in a humidified atmosphere. The medium was
563 changed by one-third every 3 days, until 30 DIV (days in vitro). In such cultures, and under control
564 conditions, neurons represented approximately 85 to 95% of the cell population; thus, for simplicity,
565 they are here referred to as "neurons." After 7 DIV, vehicle and sonicated 1B aSyn fibrils were added
566 at a final concentration of 10 nM equivalent monomeric concentration. When relevant, neurons were
567 infected at DIV 10 with AAV (adeno-associated virus) particles (multiplicity of infection, 1000)
568 carrying the cDNA of aSyn and its variants under the control of the human synapsin promoter, as
569 previously described[13]. High Content Analysis was performed after fixation and double
570 immunofluorescence staining with the conformation-dependent SynF1 antibody (mouse monoclonal,
571 BioLegend) and the human aSyn-specific MJFR1 antibody (rabbit monoclonal, Abcam) as previously
572 described on images acquired at 20× using the generic analysis module of an Incucyte S3 (Sartorius,

573 USA) with Top-Hat segmentation[13]. For quantifications the signal integral of the segmented areas in
574 each field of view was recorded. Primary neuronal cultures from C57BL/6 embryos physiologically
575 expressing endogenous mouse aSyn and not transduced with any AAV vector (**Extended data Fig. 1**)
576 were produced and analyzed similarly but after fixation at DIV24 and after revealing pS129Syn with
577 EP1536Y and human aSyn with LB509.

578 Correlative light and electron microscopy

579 The CLEM protocol was performed as previously described[26,27]. In short, 20 to 40 µm thick
580 sections were cut from perfused mouse brain on a vibratome (LEICA VT1200). Immunolabeling against
581 aSyn pathology allowed for the identification of immuno-positive sections to be used for further
582 processing with EM. For this, the sections were incubated overnight with a primary EP1536Y (Abcam)
583 antibody at 4°C followed by Alexa-conjugated secondary antibody staining together with DAPI for cell
584 nuclei identification. Fluorescence images were acquired with a Leica Thunder Tissue Imager equipped
585 with a K8 fluorescent camera. Chosen sections with strong aSyn pathology were prepared for EM by
586 post-fixing in reduced 2% osmium, thiocarbohydrazide and 2% Osmium tetroxide, followed by
587 contrasting in 2% uranyl acetate and lead aspartate treatment at 60°C. The sections were dehydrated
588 with an increasing acetone gradient, before infiltration with EMBED 812 resin for final flat embedding.
589 The hardened sections were imaged again by light microscopy and the sections overlayed with the
590 overview fluorescence map by using identifiable tissue features. Regions of interest were marked and
591 the coordinates used for laser dissection. The resulting blocks were laser cut using a Leica LMD7 and
592 glued onto a resin block. Serial sectioning with an ultra-microtome (Leica UC7) produced 120 to 200
593 nm thick tissue sections that were alternatingly collected on EM grids (slot and hexagonal grids) or
594 glass slides. Glass slides were further processed for immunohistochemistry and toluidine blue staining.

595 Light microscopy images were acquired at 40x magnification and correlated to each other for the
596 generation of an image overlay of pathology signal (IHC) and high contrast tissue morphology
597 (toluidine blue). The resulting overlays were then correlated to low magnification (640x nominal
598 magnification) EM overviews for cell identification by using identifiable tissue features both in the LM
599 and EM images. The identified pathology was finally imaged and merged at high magnification in a tile
600 acquisition series. For EM image acquisition, a Thermo Fisher Scientific (TFS) Talos F200C with a
601 CETA camera or a CM100 (Phillips) with a TVIPS F416 camera were used. LM and EM images were
602 adjusted for brightness and contrast where necessary.

603 On-grid immunogold labelling and analysis

604 EM grids with tissue sections were placed on a droplet of etching solution (1% periodic acid in
605 water, Sigma Aldrich, United States), with the sections facing down, for 2.5 minutes. Grids were washed
606 3 times for 2 minutes in ddH_2O, then washed 2 times for 2 minutes in washing buffer (stock solution of
607 10% BSA, Aurion, which was 1/50 diluted in ddH_2O), and blocked in blocking solution (Aurion) for 5

608 minutes to reduce non-specific binding. Grids were then incubated with primary antibody (EP1526Y,
609 Abcam, 1/50 diluted in washing buffer) for 60 minutes, washed 6 times for 2 minutes in blocking buffer,
610 and then incubated in a solution of gold nanoparticles with a size of 10 nm (protein A gold, Aurion,
611 1/50 diluted in washing buffer) for 90 minutes. They were washed 3 times for 2 minutes in blocking
612 solution, 3 times for 2 minutes in washing buffer, and 4 times for 1 minute in ddH_2O. Finally, grids
613 were post-stained in 1% uranyl acetate for 1 minute and washed 3 times for 10 seconds in ddH_2O.
614 Sections were imaged with a transmission electron microscope (TFS Talos L120C), operated at an
615 operating voltage of 120 kV, and images were recorded with a TFS Ceta camera.

616 Gold particles were detected automatically in the recorded EM images, using FIJI[45], by applying a
617 difference-of-gaussian filter (sigma1 = 10 nm, sigma2 = √2 • sigma1). The resulting image was
618 binarized with a manually selected threshold. Particle detections with an area smaller than 25 nm2 and
619 a circularity (4π•area/perimeter^2) below 0.8 were excluded from analysis. The local density of gold was
620 calculated as the decadic logarithm of the sum of a pixel's distance to the 15 closest neighboring gold
621 particles. The gold particle detection was implemented as a FIJI macro and the density calculation as a
622 python notebook.

623 Electron tomography and 3D reconstruction

624 Electron tomography data was collected using the Tomography software (TFS) with multi-site
625 batch acquisition on a TFS Talos F200C with tilt series covering -60º to +60º in 2º steps. Tomograms
626 were reconstructed using IMOD[46] and filtered with a non-local-means filter with Amira (TFS Amira
627 version 2021.2). For segmentation, nuclear membranes, fibrils, and other membranous parts were
628 manually annotated and traced throughout the tilt-series using Amira. Every few slices the respective
629 feature of interest was selected by drawing directly onto the image and then interpolated to generate an
630 accurate 3D volume. The final volume was visualized directly in AMIRA.

631 aSyn purification from brain homogenate

632 Extraction of the sarkosyl-insoluble fraction of a transgenic M83+/- mouse brain 16 weeks after
633 inoculation with 1B was done using the same procedure as was previously published for fibrils purified
634 from a MSA patient[11]. In brief, brain tissue was homogenized in 20 vol. (v/w) extraction buffer
635 consisting of 10 mM Tris-HCl, pH 7.5, 0.8 M NaCl, 10% sucrose and 1 mM EGTA. Homogenates were
636 brought to 2% sarkosyl and incubated for 30 min. at 37° C. Following a 10 min. centrifugation at 10,000
637 g, the supernatants were spun at 100,000 g for 20 min. The pellets were resuspended in 500 µl/g
638 extraction buffer and centrifuged at 3,000 g for 5 min. The supernatants were diluted 3-fold in 50 mM
639 Tris-HCl, pH 7.5, containing 0.15 M NaCl, 10% sucrose and 0.2% sarkosyl, and spun at 166,000 g for
640 30 min. Sarkosyl-insoluble pellets were resuspended in 100 µl/g of 30 mM Tris-HCl, pH 7.4.

641 ## Immunogold labeling and negative staining of sarkosyl purification

642 3 uL of non-diluted sample was applied to 100 mesh Ni grids with formvar support (Electron
643 Microscopy Sciences) that were glow-discharged at 15 mA for 60 seconds. After 10 minutes incubation
644 time, the grid was blotted, washed 3x 5 mins with incubation solution (0.2% BSA-c/PBS; Aurion), and
645 incubated for 1h at room temperature in a solution of aSyn-pS129 antibody (EP1536Y, Abcam,
646 ab51253) diluted 1:100 in incubation solution. The grid was washed 6x 5 min and incubated for 2h in
647 a solution containing gold nanobeads (diameter 6 nm) coupled to an anti-rabbit antibody (Aurion),
648 diluted 1:50 in incubation solution. After washing 6x 5 min in incubation solution and 3x 5min in PBS,
649 the grid was immersed in 1% uranyl acetate for 40 seconds, blotted, and air-dried. The grid was imaged
650 with a Talos transmission electron microscope at an operating voltage of 200 kV (ThermoFisher
651 Scientific).

652 ## Cryo-electron microscopy

653 **For recombinant 1B fibrils:** Cryo-EM grids were prepared using a Leica GP2 plunge freezer in a
654 BSL-2 environment at room temperature. Quantifoil 300 mesh gold grids were glow discharged in air
655 for 90s. Grids were prepared using 3 µl of 1:1 and 1:2 diluted fibril samples in preparation buffer (H2O,
656 100 mM NaCl, and 20 mM tris-HCl. pH 7.40) and vitrification by rapid freezing in liquid ethane. The
657 grids were screened for the presence of non-clustered fibers and high-resolution images were acquired
658 with an automated EPU setup on a TFS Titan Krios G4 (TFS) electron microscope equipped with a
659 cold-FEG 300kV electron source and a Falcon4i camera. 11,879 dose-fractionated movies (EER) were
660 collected with a total dose of 40 $e^-/Å^2$ at a pixel spacing of 0.66 Å at the sample level. A defocus range
661 between -0.8 µm and -1.8 µm was used during the acquisition.

662 **For purified $1B^P$ fibrils:** The sarkosyl-insoluble fraction of a transgenic M83+/- mouse brain was
663 diluted 1:3 in Tris-HCl, 50mM, 150mM NaCl, pH7.4, and 2.5 uL was applied to a Quantifoil 300 mesh
664 gold grid, coated with an additional 5-nm thick carbon layer. The grid was not glow-discharged. 30
665 seconds after applying the sample, the grid was blotted from the front side for 6 seconds and plunge-
666 frozen at room temperature and 80% humidity in a Leica GP2 plunge freezer. A total of 42,812
667 exposures was collected on a Titan Krios (TFS) electron microscope equipped with a cold-FEG 300kV
668 electron source and a Falcon4i camera. The total dose applied per movie (EER) was 50 $e^-/Å^2$ and the
669 pixel spacing was 0.732 Å. A defocus range between -0.8 µm and -2.2 µm was used during the
670 acquisition.

671 ## Helical reconstruction and model building of recombinant 1B fibrils

672 All the subsequent image processing and helical reconstruction was carried out in RELION 4.0[47]
673 (**Extended Data Fig. 13**). The recorded movies were gain corrected, motion-corrected and dose
674 weighted using RELION's own implementation of MOTIONCOR. The raw EER files were dose-
675 fractionated to a total of 32 frames (1.23 $e^-/Å^2$ per frame). After CTF estimation using Ctffind 4.1[48], the

676 aligned averages that had an estimated CTF resolution of better than 5Å were selected, resulting in a
677 total of 11,879 micrographs. aSyn fibers were picked manually as start-to-end helical segments and
678 extracted with an inter-box distance of 19 Å. Several rounds of reference-free 2D classification were
679 performed to exclude suboptimal 2D segments from further processing. The four best classes were
680 selected and binned 4 times to re-extract the segments with a bigger box size encompassing the entire
681 helical crossover. Clearly visible twisted class averages containing the entire crossover were used to
682 generate initial de novo models using the relion_helix_inimodel2d program. The most likely twist was
683 estimated from a crossover distance measured from 2D class averages and corroborated with the direct
684 measurements from micrographs.

685 The helical segments (105,496) from the entire dataset were then re-extracted with a 600 pixel box
686 size (binned by 2) comprising about 40 % of the crossover. Exclusion of the suboptimal classes after
687 2D classification resulted in 64'889 particles. Multiple rounds of 3D auto-refinement were carried out
688 to optimize the helical twist and rise, and also to check for the correct symmetry operators. This was
689 validated from the reconstructions showing clear separation of beta-strands along the helical axis.
690 Imposing a 2_1 cork-screw symmetry (pseudo two-fold symmetry) yielded the clear separation of beta-
691 strands when compared to C1 and C2 symmetries. A 3D classification without image alignment was
692 further performed to exclude the segments that gave suboptimal 3D volumes. This resulted in a final
693 51,272 particles. These were finally re-extracted at a 512 pixel (unbinned) box size and subjected to 3D
694 auto-refinement, followed by CTF refinement. Further iterations of Bayesian Polishing coupled with
695 CTF refinement yielded a map at 1.94 Å. The maps were sharpened using the standard postprocessing
696 procedure in RELION with an ad-hoc B-factor of 21 $Å^2$.

697 The atomic model for the backbone of the core of the 1B fibrils encompassing residues 34 to 95
698 was built de novo using Coot[49]. Initially, three beta-rungs were modelled in coot and were refined in
699 real-space in PHENIX[45]. Finally, these chains were extended to 9 beta-rungs per protofilament and
700 refined in tandem with phenix.real_space_refine and in coot to improve the Ramachandran and
701 Geometric statistics. NCS and secondary structural restraints were included during the iterative
702 refinement process.

703 Helical reconstruction and model building of purified $1B^P$ fibrils

704 Because most of the 42,812 collected movies did not contain any fibrillar material, they were first
705 imported into cryoSPARC[50], motion corrected, and manually inspected using a
706 "manually_curate_exposures" job. After manual inspection, 156 movies with intact, twisting fibrils
707 were selected for further processing in RELION4[47]. They were dose-fractionated in RELION's
708 MOTIONCOR implementation with 24 frames per fraction, corresponding to a dose of 1.28 e-/Å2 per
709 frame, and CTF-corrected using Ctffind 4.1[48]. Fibrils were found to cluster into three morphological
710 groups (Extended Data Fig. 8). Manual picking was done in three rounds, using 209, 7 and 40 movies

711 for the three respective groups. After extraction with binning of 2 and an inter-box distance of 14.4 Å
712 (3 asymmetrical units), several rounds of 2D classification were applied. One of the three morphological
713 groups (40 movies) yielded 2D classes for which a clear twist and monomer separation was visible,
714 while the other two morphological groups did not yield any interpretable result.

715 Using the 2D class averages of the one usable group, a de-novo initial model was generated with
716 relion_helix_inimodel2d. Particles were re-extracted with a box size of 800 and a binning of 2, and after
717 multiple rounds of 2D classification, 1913 particles were kept for a 3D classification job with 1 class
718 and the de-novo inimodel2d reconstruction as initial model. When a fibril backbone was visible, the
719 regularisation parameter (T) was gradually increased to 12 over the course of 50 iterations, and the
720 result was used for a 3D refinement with a tau2 fudge factor of 2 to search for the optimal helical rise
721 and twist. After CTF refinement and postprocessing, a 3D map at a resolution of 3.8Å was obtained.

722 To build the 1BP atomic model, one beta rung of the 1B model was fitted into the 1BP density
723 using a rigid-body fit in ChimeraX[51], followed by a jiggle fit and all-atom refinement in Coot[49]. Position
724 53 was mutated into a threonine and the model was extended to five beta rungs, which were refined
725 together in phenix.real_space_refine. After refinement, the outer two beta rungs were removed in Coot.
726 NCS and secondary structural restraints were included during the iterative refinement process.

727 FLIM of aSyn inclusion pathology

728 h-FTAA was synthesised and purified as previously described[36] and paraffin-embedded sections
729 of 1B-injected wild-type mouse brains (129SV) and regions from human donor brain samples were
730 stained with h-FTAA and processed for immunofluorescence against pS129Syn (EP1536Y) for the
731 inclusions or against human aSyn (LB509) for the 1B inoculate and counterstained with the nuclear
732 marker DAPI as previously described[37]. To confirm previous observations regarding the capability of
733 h-FTAA to discriminate Lewy bodies and GCIs using FLIM[37], human brain samples from one MSA
734 and one DLB subject were obtained from the repository of the University Hospital of Bordeaux (CRB-
735 BBS). Subjects or a legal representative had given informed written consent for collecting and using
736 clinical and post-mortem data, and mandatory regulatory approval for post-mortem brain tissue use was
737 obtained (MESR AC-2024-6715, DC-2024-6714). FLIM was performed on a Leica SP8 WLL2
738 confocal microscope on an inverted stand DMI6000 (Leica Microsystems, Mannheim, Germany), using
739 HCX Plan Apo CS2 63X oil NA 1.40 objective. This microscope was equipped with a pulsed white
740 light laser 2 (WLL2) with freely tunable excitation from 470 to 670 nm (1 nm steps) and also a diode
741 laser at 405 nm. A FALCON module enabled us to perform FLIM measurement based on Time
742 Correlated Single Photon Counting (TCSPC) technique. The FLIM analysis was done using phasor plot
743 representation of the data and was focused on pS129Syn-positive inclusions[37], or LB509-positive
744 regions in the case of the 1B inoculate. For Gallyas silver impregnation, mouse brain sections were

processed as previously described[38]using a commercial Gallyas staining kit (Morphisto, Offenbach am Main, Germany).

Atomic force microscopy

1B aSyn fibrils were deposited on a freshly cleaved mica disk and left to adhere for 15 minutes in a humid chamber at room temperature. The sample was rinsed and imaged in saline buffer solution (H_2O, HEPES 20 mM, NaCl 100 mM, pH 7.4). AFM imaging was performed using the Dimension FastScan setup (Bruker) operating in PeakForce Quantitative Nano-Mechanics (PF-QNM) mode in liquid at room temperature, using sharp SNL-C probes (Bruker, Silicon tips on silicon nitride cantilevers), with a nominal spring constant of 0.24 N/m, a resonance frequency of 56 kHz, and a nominal tip radius of 2 nm. Fibrils were imaged with a peak force frequency of 1 kHz, a scan rate of 0.5 Hz and a constant setpoint force of 500 pN. Image analysis was performed using Nanoscope analysis (Bruker).

References

1. Poewe, W. *et al.* Multiple system atrophy. *Nat. Rev. Dis. Primer* **8**, 56 (2022).
2. Jellinger, K. A. Multiple System Atrophy: An Oligodendroglioneural Synucleinopathy1. *J. Alzheimers Dis.* **62**, 1141–1179 (2018).
3. Dickson, D. W., Lin, W., Liu, W. & Yen, S. Multiple System Atrophy: A Sporadic Synucleinopathy. *Brain Pathol.* **9**, 721–732 (1999).
4. Arima, K. *et al.* NACP/α-synuclein immunoreactivity in fibrillary components of neuronal and oligodendroglial cytoplasmic inclusions in the pontine nuclei in multiple system atrophy. *Acta Neuropathol. (Berl.)* **96**, 439–444 (1998).
5. Dickson, D. *et al.* Glial cytoplasmic inclusions (GCI) of multiple system atrophy (MSA) contain α-synuclein. *Mov. Disord.* **13**, 128 (1998).
6. Wakabayashi, K. *et al.* Accumulation of α-synuclein/NACP is a cytopathological feature common to Lewy body disease and multiple system atrophy. *Acta Neuropathol. (Berl.)* **96**, 445–452 (1998).
7. Tu, P. *et al.* Glial cytoplasmic inclusions in white matter oligodendrocytes of multiple system atrophy brains contain insoluble α-synuclein. *Ann. Neurol.* **44**, 415–422 (1998).
8. Gai, W., Power, J., Blumbergs, P. & Blessing, W. Multiple-system atrophy: a new α-synuclein disease? *The Lancet* **352**, 547–548 (1998).
9. Watts, J. C. *et al.* Transmission of multiple system atrophy prions to transgenic mice. *Proc. Natl. Acad. Sci.* **110**, 19555–19560 (2013).
10. Prusiner, S. B. *et al.* Evidence for α-synuclein prions causing multiple system atrophy in humans with parkinsonism. *Proc. Natl. Acad. Sci.* **112**, (2015).
11. Schweighauser, M. *et al.* Structures of α-synuclein filaments from multiple system atrophy. *Nature* **585**, 464–469 (2020).
12. Lövestam, S. *et al.* Seeded assembly in vitro does not replicate the structures of α-synuclein filaments from multiple system atrophy. *FEBS Open Bio* **11**, 999–1013 (2021).
13. De Giorgi, F. *et al.* Novel self-replicating α-synuclein polymorphs that escape ThT monitoring can spontaneously emerge and acutely spread in neurons. *Sci. Adv.* **6**, eabc4364 (2020).
14. De Giorgi, F. *et al.* Neurons with Cat's Eyes: A Synthetic Strain of α-Synuclein Fibrils Seeding Neuronal Intranuclear Inclusions. *Biomolecules* **12**, 436 (2022).
15. De Nuccio, F. *et al.* Oligodendrocytes Prune Axons Containing α-Synuclein Aggregates In Vivo: Lewy Neurites as Precursors of Glial Cytoplasmic Inclusions in Multiple System Atrophy? *Biomolecules* **13**, 269 (2023).
16. Papp, M. I. & Lantos, P. L. The distribution of oligodendroglial inclusions in multiple system atrophy and its relevance to clinical symptomatology. *Brain* **117**, 235–243 (1994).

17. Kato, S. *et al.* Argyrophilic ubiquitinated cytoplasmic inclusions of Leu-7-positive glial cells in olivopontocerebellar atrophy (multiple system atrophy). *Acta Neuropathol. (Berl.)* **82**, 488–493 (1991).

18. Papp, M. I. & Lantos, P. L. Accumulation of tubular structures in oligodendroglial and neuronal cells as the basic alteration in multiple system atrophy. *J. Neurol. Sci.* **107**, 172–182 (1992).

19. Spillantini, M. G., Crowther, R. A., Jakes, R., Hasegawa, M. & Goedert, M. α-Synuclein in filamentous inclusions of Lewy bodies from Parkinson's disease and dementia with Lewy bodies. *Proc. Natl. Acad. Sci.* **95**, 6469–6473 (1998).

20. Gai, W. P., Power, J. H. T., Blumbergs, P. C., Culvenor, J. G. & Jensen, P. H. α-Synuclein Immunoisolation of Glial Inclusions from Multiple System Atrophy Brain Tissue Reveals Multiprotein Components. *J. Neurochem.* **73**, 2093–2100 (1999).

21. Peelaerts, W. *et al.* α-Synuclein strains cause distinct synucleinopathies after local and systemic administration. *Nature* **522**, 340–344 (2015).

22. Uemura, N. *et al.* Slow Progressive Accumulation of Oligodendroglial Alpha-Synuclein (α-Syn) Pathology in Synthetic α-Syn Fibril-Induced Mouse Models of Synucleinopathy. *J. Neuropathol. Exp. Neurol.* **78**, 877–890 (2019).

23. Lin, W.-L., DeLucia, M. W. & Dickson, D. W. α-Synuclein immunoreactivity in neuronal nuclear inclusions and neurites in multiple system atrophy. *Neurosci. Lett.* **354**, 99–102 (2004).

24. Woulfe, J. M. Abnormalities of the nucleus and nuclear inclusions in neurodegenerative disease: a work in progress. *Neuropathol. Appl. Neurobiol.* **33**, 2–42 (2007).

25. Nishie, M., Mori, F., Yoshimoto, M., Takahashi, H. & Wakabayashi, K. A quantitative investigation of neuronal cytoplasmic and intranuclear inclusions in the pontine and inferior olivary nuclei in multiple system atrophy. *Neuropathol. Appl. Neurobiol.* **30**, 546–554 (2004).

26. Shafiei, N. *et al.* Correlative light and electron microscopy for human brain and other biological models. *Nat. Protoc.* 1–30 (2025) doi:10.1038/s41596-025-01153-9.

27. Shahmoradian, S. H. *et al.* Lewy pathology in Parkinson's disease consists of crowded organelles and lipid membranes. *Nat. Neurosci.* **22**, 1099–1109 (2019).

28. St-Pierre, M.-K. *et al.* Ultrastructural characterization of dark microglia during aging in a mouse model of Alzheimer's disease pathology and in human post-mortem brain samples. *J. Neuroinflammation* **19**, 235 (2022).

29. Tremblay, M.-È. Microglial functional alteration and increased diversity in the challenged brain: Insights into novel targets for intervention. *Brain Behav. Immun. - Health* **16**, 100301 (2021).

30. Böing, C. *et al.* Distinct ultrastructural phenotypes of glial and neuronal alpha-synuclein inclusions in multiple system atrophy. *Brain* awae137 (2024) doi:10.1093/brain/awae137.

31. Hass, E. W. *et al.* Robust α-synuclein pathology in select brainstem neuronal populations is a potential instigator of multiple system atrophy. *Acta Neuropathol. Commun.* **9**, 80 (2021).
32. Guerrero-Ferreira, R. *et al.* Cryo-EM structure of alpha-synuclein fibrils. *eLife* **7**, (2018).
33. Tao, Y. *et al.* Structural mechanism for specific binding of chemical compounds to amyloid fibrils. *Nat. Chem. Biol.* **19**, 1235–1245 (2023).
34. Shahnawaz, M. *et al.* Discriminating α-synuclein strains in Parkinson's disease and multiple system atrophy. *Nature* **578**, 273–277 (2020).
35. Beton, J. G. *et al.* Cooperative amyloid fibre binding and disassembly by the Hsp70 disaggregase. *EMBO J.* **41**, e110410 (2022).
36. Rasmussen, J. *et al.* Amyloid polymorphisms constitute distinct clouds of conformational variants in different etiological subtypes of Alzheimer's disease. *Proc. Natl. Acad. Sci.* **114**, 13018–13023 (2017).
37. Klingstedt, T. *et al.* Luminescent conjugated oligothiophenes distinguish between α-synuclein assemblies of Parkinson's disease and multiple system atrophy. *Acta Neuropathol. Commun.* **7**, 193 (2019).
38. Uchihara, T. *et al.* Silver stainings distinguish Lewy bodies and glial cytoplasmic inclusions: comparison between Gallyas-Braak and Campbell-Switzer methods. *Acta Neuropathol. (Berl.)* **110**, 255–260 (2005).
39. Holec, S. A. M. *et al.* The E46K mutation modulates α-synuclein prion replication in transgenic mice. *PLOS Pathog.* **18**, e1010956 (2022).
40. Woerman, A. L. *et al.* Familial Parkinson's point mutation abolishes multiple system atrophy prion replication. *Proc. Natl. Acad. Sci.* **115**, 409–414 (2018).
41. Luk, K. C. *et al.* Molecular and Biological Compatibility with Host Alpha-Synuclein Influences Fibril Pathogenicity. *Cell Rep.* **16**, 3373–3387 (2016).
42. Balana, A. T. *et al.* O-GlcNAc forces an α-synuclein amyloid strain with notably diminished seeding and pathology. *Nat. Chem. Biol.* **20**, 646–655 (2024).
43. Oueslati, A., Paleologou, K. E., Schneider, B. L., Aebischer, P. & Lashuel, H. A. Mimicking Phosphorylation at Serine 87 Inhibits the Aggregation of Human α-Synuclein and Protects against Its Toxicity in a Rat Model of Parkinson's Disease. *J. Neurosci.* **32**, 1536–1544 (2012).
44. De Chaumont, F. *et al.* Icy: an open bioimage informatics platform for extended reproducible research. *Nat. Methods* **9**, 690–696 (2012).
45. Afonine, P. V. *et al.* Real-space refinement in *PHENIX* for cryo-EM and crystallography. *Acta Crystallogr. Sect. Struct. Biol.* **74**, 531–544 (2018).
46. Kremer, J. R., Mastronarde, D. N. & McIntosh, J. R. Computer Visualization of Three-Dimensional Image Data Using IMOD. *J. Struct. Biol.* **116**, 71–76 (1996).
47. Kimanius, D., Dong, L., Sharov, G., Nakane, T. & Scheres, S. H. W. New tools for automated cryo-EM single-particle analysis in RELION-4.0. *Biochem. J.* **478**, 4169–4185 (2021).

48. Rohou, A. & Grigorieff, N. CTFFIND4: Fast and accurate defocus estimation from electron micrographs. *J. Struct. Biol.* **192**, 216–221 (2015).

49. Emsley, P. & Cowtan, K. *Coot* : model-building tools for molecular graphics. *Acta Crystallogr. D Biol. Crystallogr.* **60**, 2126–2132 (2004).

50. Punjani, A., Rubinstein, J. L., Fleet, D. J. & Brubaker, M. A. cryoSPARC: algorithms for rapid unsupervised cryo-EM structure determination. *Nat. Methods* **14**, 290–296 (2017).

51. Goddard, T. D. *et al.* UCSF ChimeraX: Meeting modern challenges in visualization and analysis. *Protein Sci. Publ. Protein Soc.* **27**, 14–25 (2018).

52. Jaccard, P. Étude comparative de la distribution florale dans une portion des Alpes et du Jura. *Bull. Société Vaudoise Sci. Nat.* **37**, 547 (1901).

Acknowledgements

Cryo-EM data were in part collected at the Dubochet Center for Imaging (DCI) in Lausanne. The DCI-Lausanne is a joint initiative of the EPFL and the Universities of Lausanne and Geneva. We thank Alex Myasnikov from the DCI-Lausanne for expert technical assistance in cryo-EM data collection, Ænora Letourneur and Fabrizio Cavallaro for their help with primary culture and immunofluorescence, Francesca Serinelli for support with paraffin histology, Sandra Dovero and Nathalie Biendon for support with Pannoramic™ slide scanning, Benjamin Dehay for sharing the AAV-Syn mutants vectors, Marion Picquemal for support with animal surgery, Latifa Lakhdar, Aude de César and Damien Gaillard for animal experiments in M83 mice, Sabrina Lacomme and Fabrice Cordelières from the Bordeaux Imaging Center for their help with sample fixation for CLEM and with the Zeiss CD7 platform respectively. Room-temperature EM was collected in part at the electron microscopy facility (EMF) of the University of Lausanne. We thank Christel Genoud and the whole EMF team for their assistance throughout the project.

Author contributions

FI and HS conceived and managed the project. FI, HS, FDG, DDL and TB designed the experiments. DB, FI and HS wrote the first version of the manuscript. DB, LvdH and IM performed the sample preparation and image acquisition for cryo-EM. DB and LvdH performed the structural analysis. MK and FDN performed in vivo experiments in 129SV wild-type mice and neuropathology stainings. DB and AJL performed the CLEM experiments. DB and LvdH performed the immunogold labelling, and LvdH the immunogold analysis. HdLS, FDG and FI produced aSyn and fingerprinted 1B. JV performed the analyses of the in vivo experiments in transgenic M83 mice and purified the fibrils from brains. CF performed the AFM of 1B fibrils. HdLS, MB and AL SEC-purified aSyn. MLA performed the surgery and AR the post-mortem brain perfusion/fixation of C57BL/6 wild-type mice. WM and M-HC certified and provided the sections from MSA and DLB patient donors. CP, FDG, FI and HdLS performed the FLIM experiments. KPRN synthetized h-FTAA. FL helped in setting up the fibril isolation procedures from mouse brains. EB, FL and LB participated in early characterizations of 1B. FDG and FI performed the HCA experiments, as well as the confocal and slide scanning neuropathology analyses of wild-type and M83 mice. All authors contributed to the writing of the manuscript.

Data availability

For the 1B and $1B^P$ respectively, the raw cryo-EM images are available at the EMPIAR database, accession numbers EMPIAR-12012 and EMPIAR-XXXXX, respectively. The reconstructed 3D maps are available at the EMDB database, accession numbers EMD-19986 and EMD-54402. The atomic models are available at the PDB database, accession numbers PDB-9EUU and PDB-9ZRF.

Funding

This work was supported by the Swiss National Science Foundation, Grants 310030_188548 & 10002679, the Swiss Parkinson Foundation, the Department of Excellence Initiative of the Italian Ministry of Research, the Innovative Medicines Initiative 2 Joint Undertaking under grant agreement No 116060 (IMPRiND), supported by the European Union's Horizon 2020 research and innovation program and EFPIA, and the French Agence Nationale de la Recherche, Grants ANR-21-CE18-0045-03, ANR-22-CE16-0002 & ANR-24-CE93-0003.

Ethical compliance

All experimental procedures were conducted in accordance with the European Communities Council Directive (2010/63/EU) for care of laboratory animals. The animal study protocol was approved by the animal experimentation ethics committee of the University of Bordeaux and validated by the French Ministry of Research (protocol APAFIS #33147-2021091711598830 v6, 2021–2026). For brain tissue sections from human origin, subjects or a legal representative had given informed written consent for collecting and using clinical and post-mortem data, and mandatory regulatory approval for post-mortem brain tissue use was obtained (MESR AC-2024-6715, DC-2024-6714)

Competing interests

Domenic Burger is an employee of F. Hoffmann - La Roche Ltd. The presented work was conducted prior to his employment and had no influence on the design, analysis, interpretation or reporting of the results herein.

Extended data figures

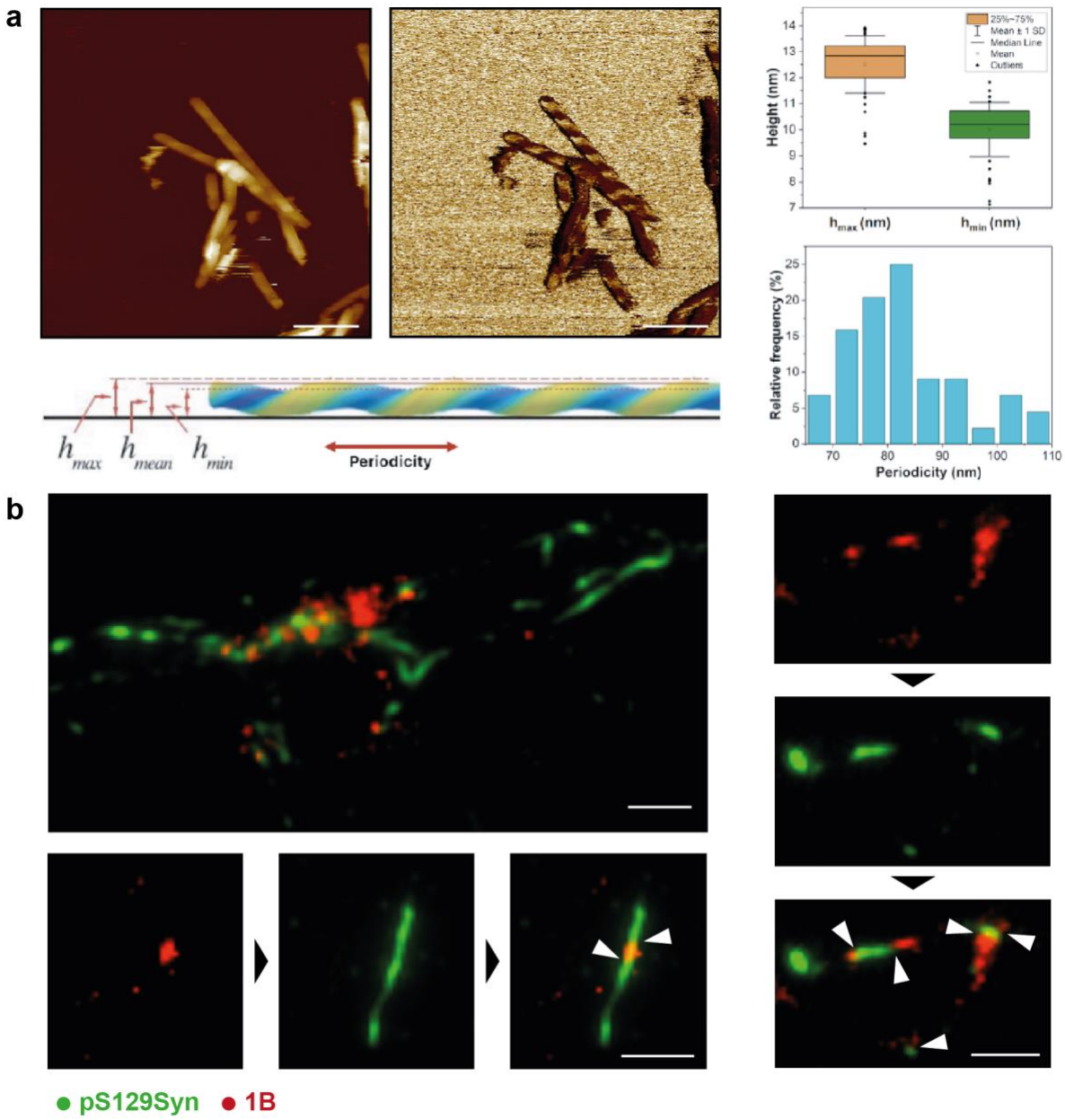

Extended Data Fig. 1 | AFM appearance of 1B fibrils and early formation of "seeding junctions" between 1B and the nascent seeded inclusions in neuronal processes. a. Topographical (Height Sensor) and nano-mechanical mapping (Derjaguin-Müller-Toporov (DMT) Modulus, log representation) of 1B fibrils using atomic force microscopy (AFM) in liquid. Right panels: fibril height values (see cartoon for definitions) for n = 103 measurements, and left twist periodicity for n = 12 fibrils. Scale bars = 240 nm. **b.** Examples of early "seeding junctions" between 1B and the nascent seeded inclusions in neuronal processes two weeks post seeding (arrowheads = seeding junctions). 96-well pooled primary cultures of cortical neurons from 8 wild-type mouse embryos (C57BL/6) were challenged at day-in-vitro 7 (DIV7) with 10 nM 1B fibrils (equivalent aSyn monomer concentration). The neurons were fixed two weeks later at DIV24 and both the 1B input fibril remnants (red) and the seeded aSyn inclusions (green) were revealed. Indeed, we took advantage of the fact that synthetic 1B is made of human aSyn and thus that it can be specifically recognized by LB509 which is a human aSyn-specific antibody. Mouse aSyn is LB509 negative. The seeded

944 inclusions were revealed contemporary using EP1536Y against pS129 aSyn. This allowed us to observe
945 many seeding junctions in the neuronal processes (arrows). Note that in a majority of images, and in
946 agreement with early reports, the seed (1B in our case) is not phosphorylated, and that the growing seeded
947 inclusions are instead pS129Syn-positive. At later time points 1B seeds get overwhelmed and are no longer
948 discernible in the mass of the seeded inclusions (not shown). The disappearance of the 1B seeds is even
949 faster *in vivo* (within a few days, not shown). (scale bars = 10 µm)

950

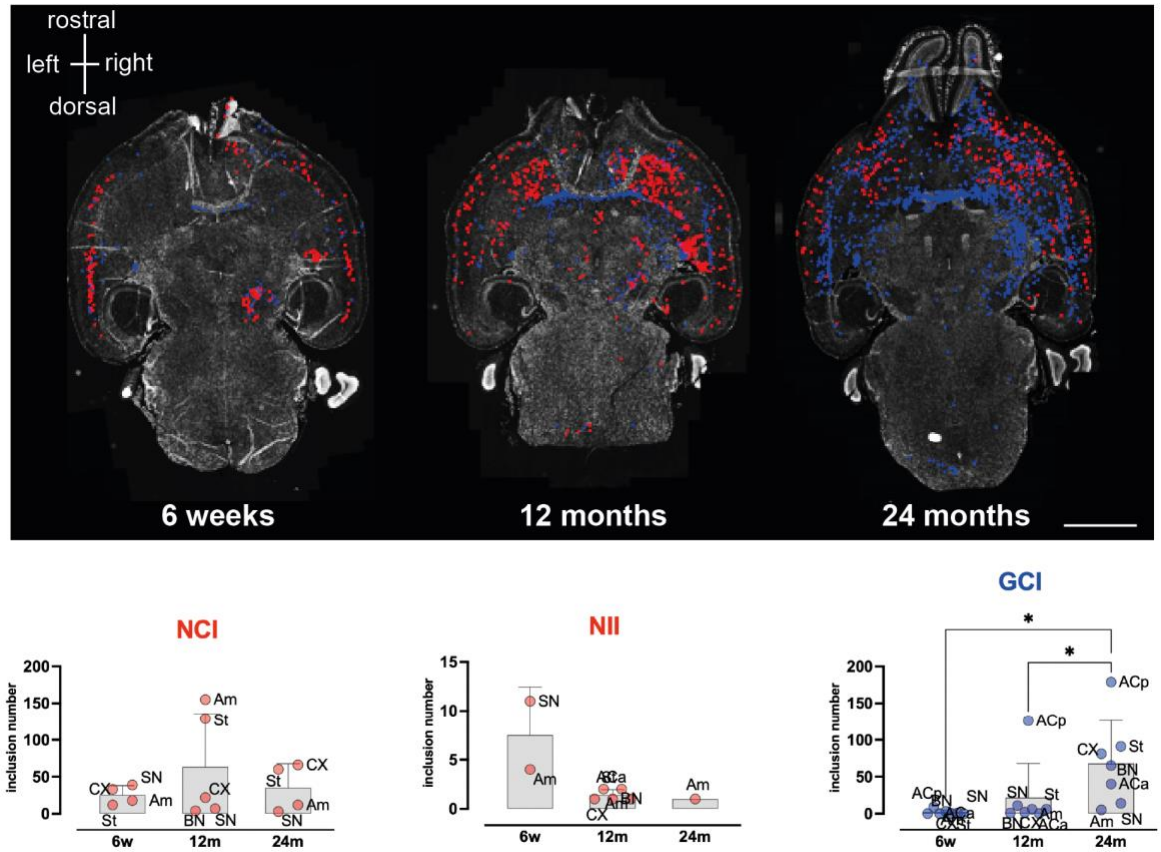

Extended Data Fig. 2 | Somatic inclusions seeded by 1B *in vivo* observed at 3 time points. Depending on the neuroanatomical structure and the time point under consideration, experimental GCIs (blue) coexisted with a variable load of surrounding neuronal somatic aSyn inclusions (NCIs & NIIs, both in red), which represent the forefront of the somatic aSyn pathology at earlier time points to progressively make way to a growing population of GCIs. The brain sections are the ones shown in **Fig. 1f** and were stained with DAPI for nuclei, Sox10 to identify the oligodendrocytes, and EP1536Y for pS129Syn. All the inclusions were manually annotated according to these 3 markers. Anatomical quantification regions were as follows: Am: amygdala; ACa: anterior limb of the anterior commissure; ACp: posterior limb of the anterior commissure; BN: bed nucleus of the stria terminalis; CX: cortex; St: caudate putamen (striatum); SN: substantia nigra. In agreement with visual perception, the neuronal inclusions peak at 12 months in the Caudate putamen (St) and the Amygdala (AM) to decrease at 24 months, while the GCIs suddenly increase in the posterior limb of the Anterior Commissure at 12 months, and then in most of the other brain regions. Note that NIIs form especially early (at 6 weeks) in the SN and the AM, then in other regions at 12 months, to eventually disappear but in the AM at 24 months. The mean number of GCIs in all regions at 24 months is significantly increased compared to the 2 other time points (* = one-way ANOVA $p<0.05$)

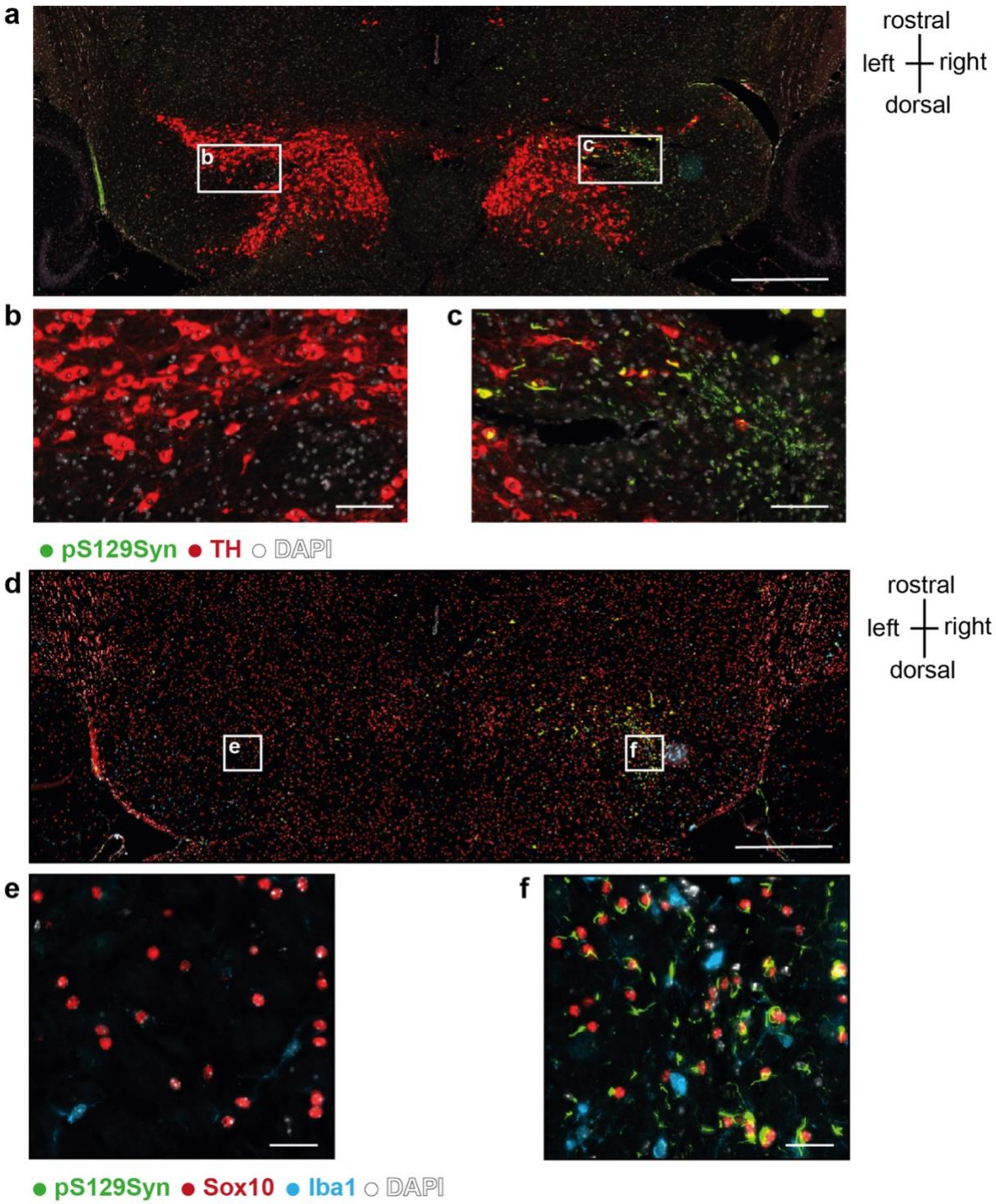

Extended Data Fig. 3 | Semi-topographic view of a horizontal brain section from a C57BL/6 wild-type mouse injected 17 months earlier at the level of its right substantia nigra (SN) with 1B fibrils . a. aSyn inclusions are revealed using the anti-phospho aSyn antibody #64 (green), dopaminergic neurons using an anti-tyrosine hydroxylase antibody (TH, red) and nuclei using DAPI (white). Left and right SNs are visible with a loss of immunoreactivity symmetry with depletion of TH-positive neurons and unilateral aSyn inclusions on the right side. The TH-depleted/aSyn inclusion-rich region is enlarged in **b**, the corresponding left region is enlarged in **c. d.** Semi-topographic view of the n+1 horizontal section consecutive to (a). aSyn inclusions in green (anti-phospho aSyn antibody #64), OLs in red (anti-Sox10 antibody), microglial cells in blue (anti -Iba1) and nuclei in white (DAPI). The right SN enlarged in f contains numerous GCIs and sparse

977 microglial cells. **e**. **f.** Enlarged view of the corresponding region of the left SN. Scale bars: a, d = 500 µm; b,
978 c = 100µm; e, f = 20 µm

979

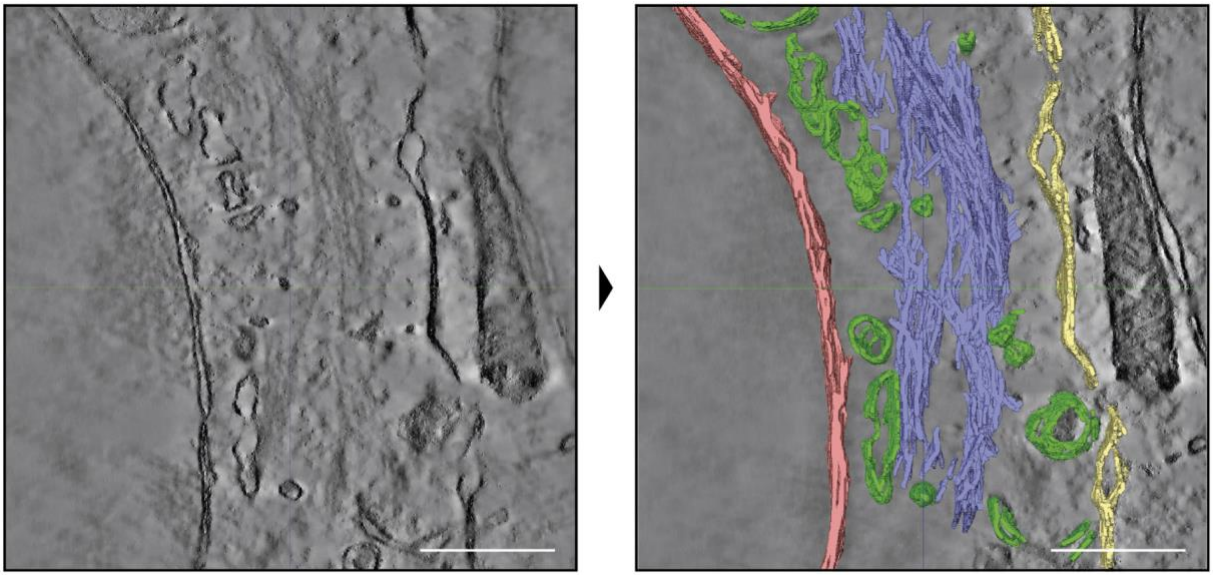

Extended Data Fig. 4 | Tomogram segmentation of aSyn fibril bundles. Tomograms were manually segmented to visualize the fibril bundling (blue), the nuclear membrane (red), the cell membrane (yellow), and other membranous compartments (green). Left: A slice view of the reconstructed tomogram with applied filtering to better visualize the filaments within the inclusion. Right: Overlay with 3D-segmented elements. Scale bars = 500 nm.

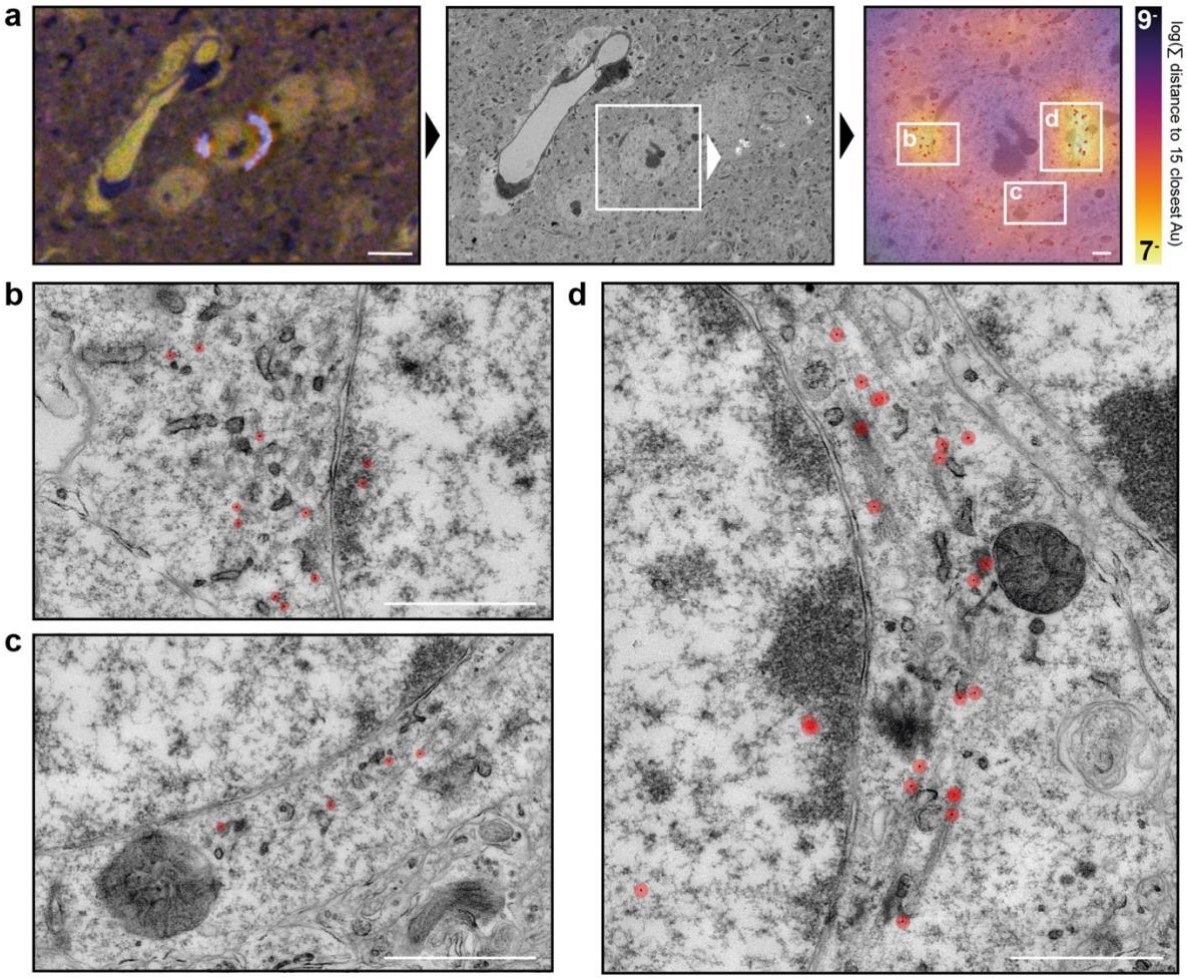

Extended Data Fig. 5 | Immunogold analysis against aSyn in the mouse brain. a. Immunohistochemistry (IHC) labelling indicates two regions with aSyn pathology wrapping around the nucleus of an affected cell. The correlated EM image with on-grid immunolabelling against aSyn shows an increase of gold particles in comparison to the background as indicated by the heatmap. Higher magnifications are indicated by the labelled boxes. **b.** Zoomed view on the left side of the nucleus, highlighted are the gold particles in red, laying on top of dispersed fibrils. **c.** Lower part of the pathology from the right side of the cell. The zoomed area shows four gold particles laying on top of fibril pathology. **d.** Zoom of right-side pathology, with highest concentration of gold particles, laying on fibril bundles. Scale bars = 5 µm for overlay and low magnification EM, 1 µm for heatmap and zoomed EM views.

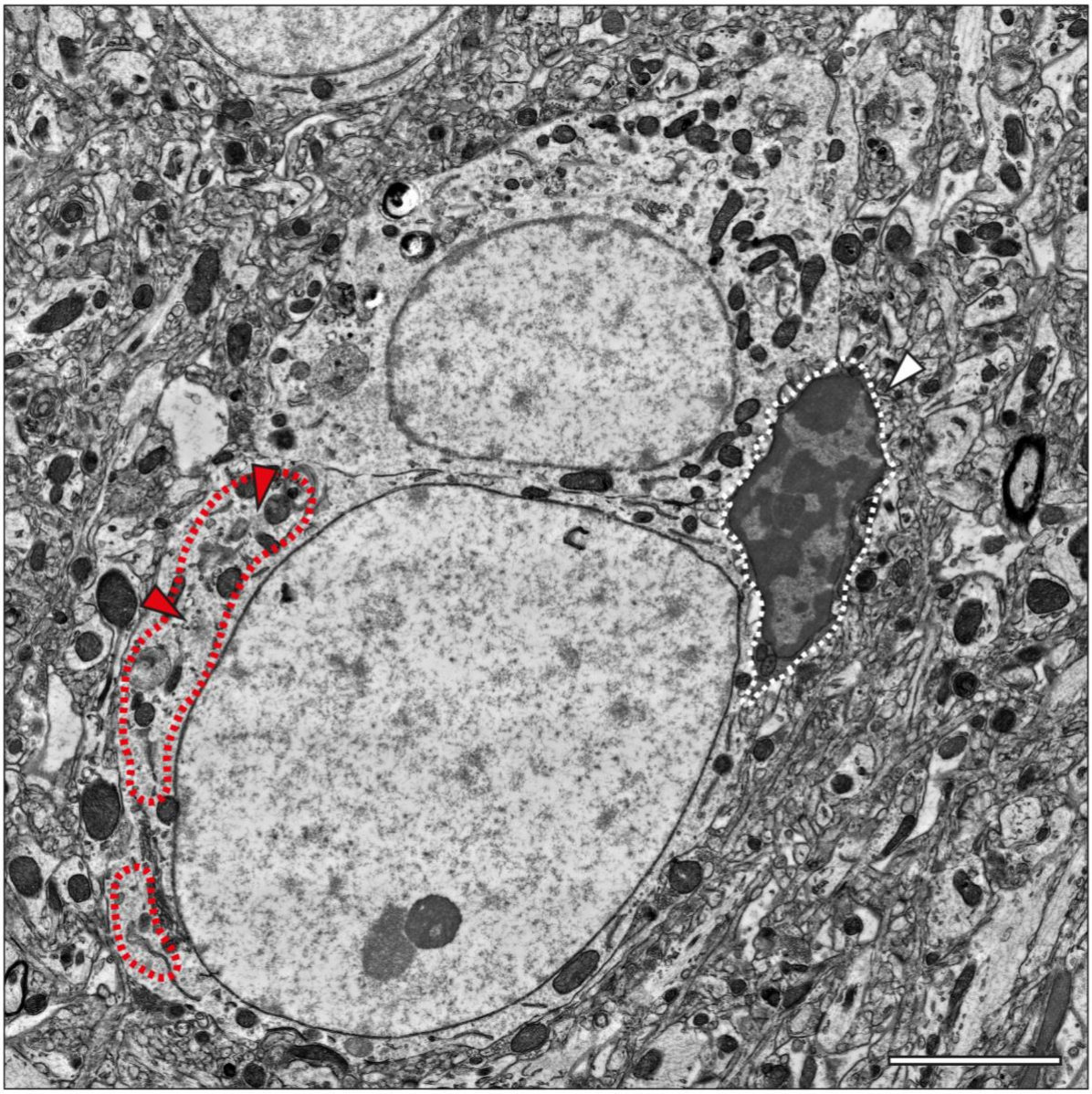

Extended Data Fig. 6 | Pathological oligodendrocyte in direct contact with other cells. Cells with a distinct morphology, previously described as "dark microglia", can be found in close proximity or in direct contact with pathological cells (white arrowhead). The total cell volume of the dark microglia is indicated by the white dashed line. In this specific case the fibrillar pathology of the oligodendrocyte appears in a dispersed arrangement with two smaller clusters (red arrowheads). Total area of immunopositive IHC is indicated by a red dashed line. Both oligodendrocytes contain aSyn pathology however for the upper cell volume it is not visible in this EM slice (based on IHC positive signal from other EM grids). Scale bar = 3 µm.

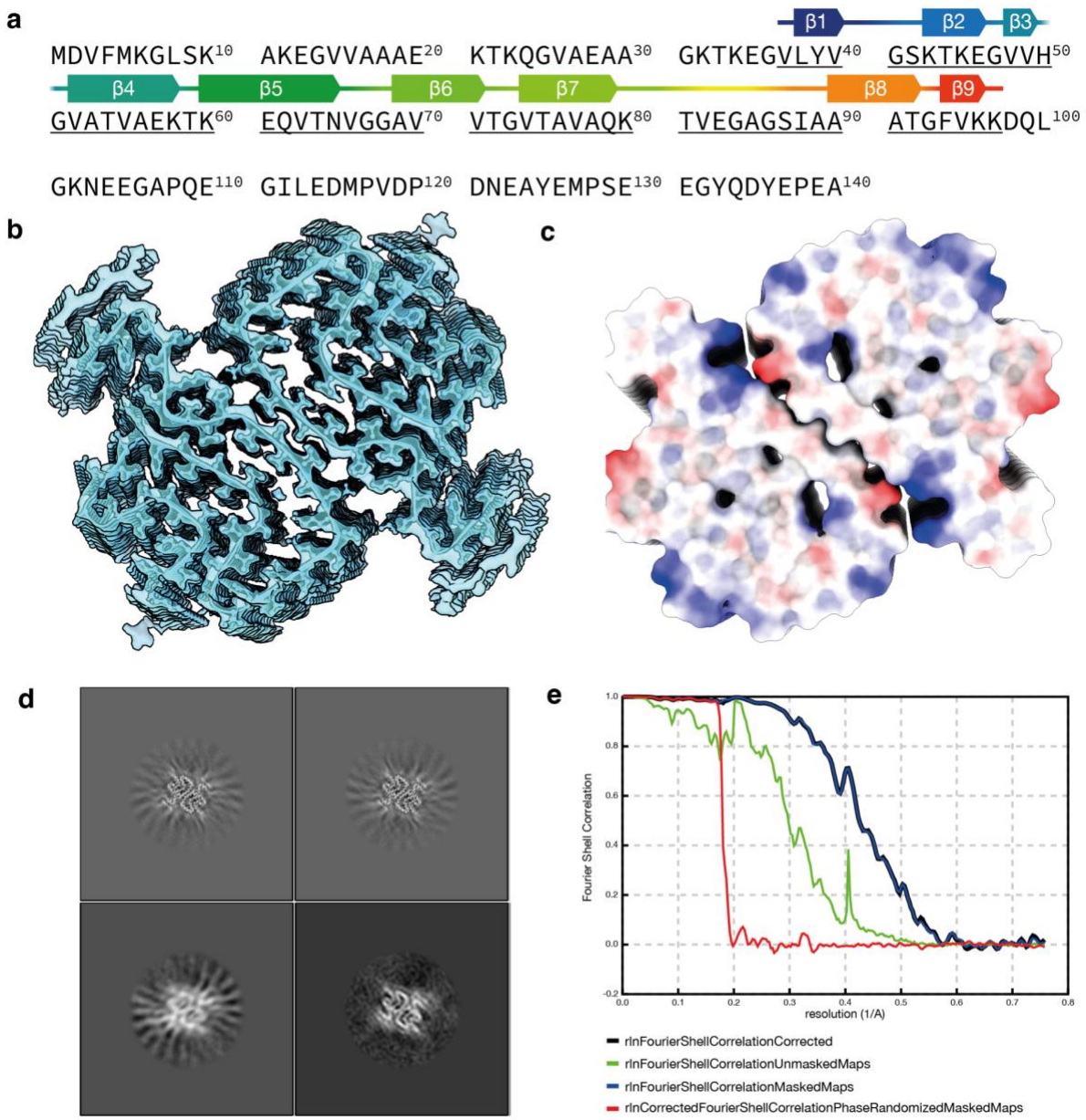

Extended Data Fig. 7 | Further structure analysis of the 1B conformation. a. Sequence of aSyn with the resolved density indicated by the colored line. Secondary beta-sheets are indicated in consecutive order by β1-9. **b.** The final 1.94 Å map of 1B with the model fitted. The extra densities flanking the starting stretches were not built. **c.** Surface color representation by the electrostatic potential. **d.** 3D class averages from early processing stages indicate a homogeneous sample. **e.** FSC curve of 1B with cutoff at 0.143 of the final map at 1.94 Å.

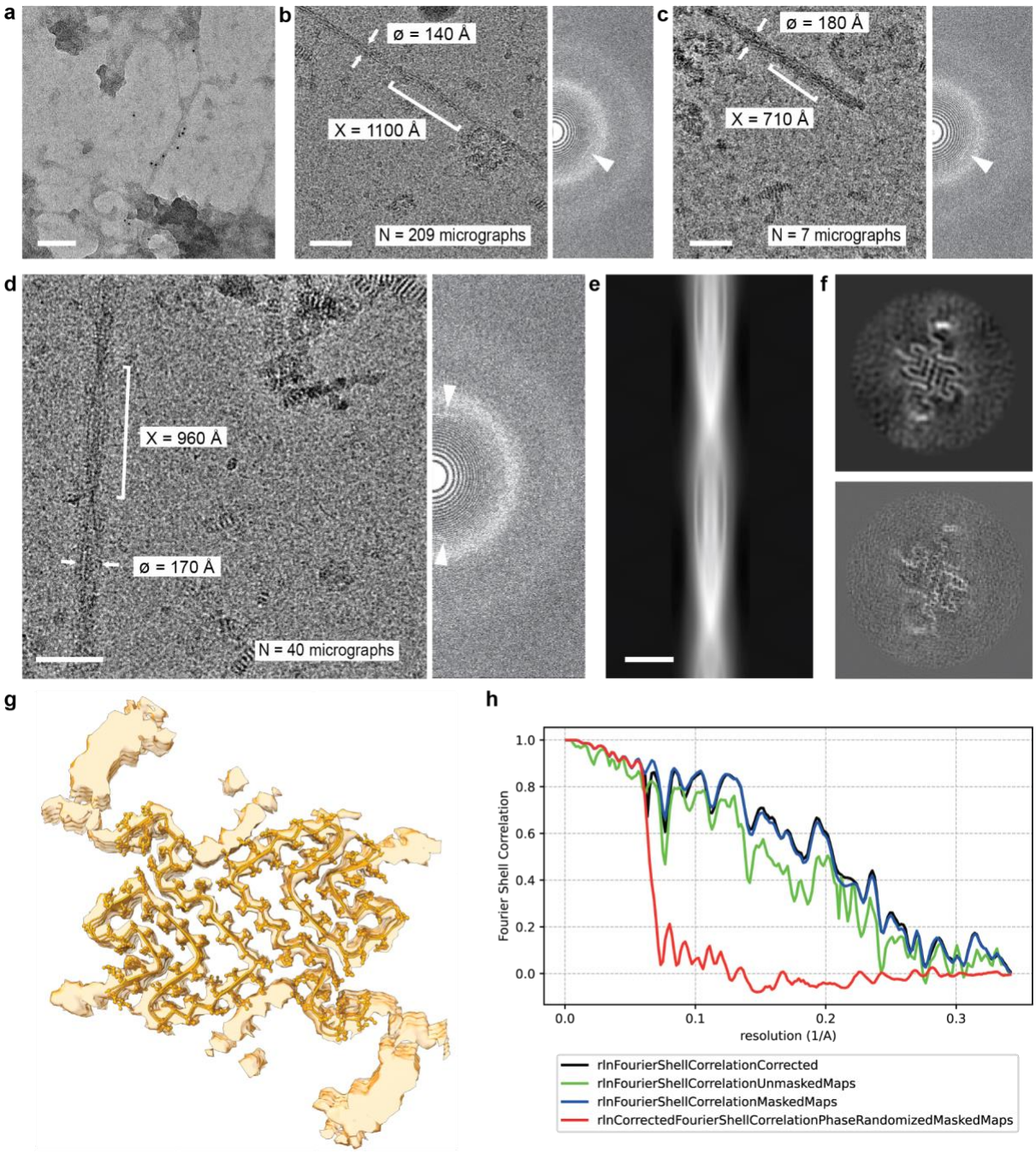

Extended Data Fig. 8 | CryoEM analysis of 1B^{P} fibrils purified from a tg M83+/- mouse brain seeded with 1B fibrils. (a) Negative staining combined with immunolabeling against aSyn-pS129 reveals that, amid aggregated precipitates, individual aSyn fibrils are present. **(b-d)** Cryo-EM micrographs (left) of intact fibrils observed in the sarkosyl-insoluble fraction, together with their power spectral density (right). A reflection at ~4.8Å (white arrowheads) reveals that these are amyloid fibrils. Presumably, the fibrils in (b), (c) and (d) represent 3 distinct conformations as can be seen from their different morphologies, although the particle counts are too low to verify this with a 3D reconstruction. The crossover distance (X) and largest diameter (ø) are indicated, as well as the number of micrographs (N) displaying at least one crossover of a fibril of the same morphological group as determined by manual inspection. The fibrils in group (d) did eventually yield a 3.8Å structure, while those in groups (b) and (c) did not yield any structure despite many attempts. **(e)** Reprojection of the 2D inimodel constructed from 2'492 particles selected from group (d). **(f)** 3D helical reconstruction of 1'913 particles selected from group (d), before (top) and after (bottom) post-processing in

RELION. **(g)** The final 3.8Å map of $1B^P$ with the model fitted. **(h)** FSC curve of $1B^P$. Scalebars: (a) 100 nm, (b-d) 50 nm, (e) 20 nm.

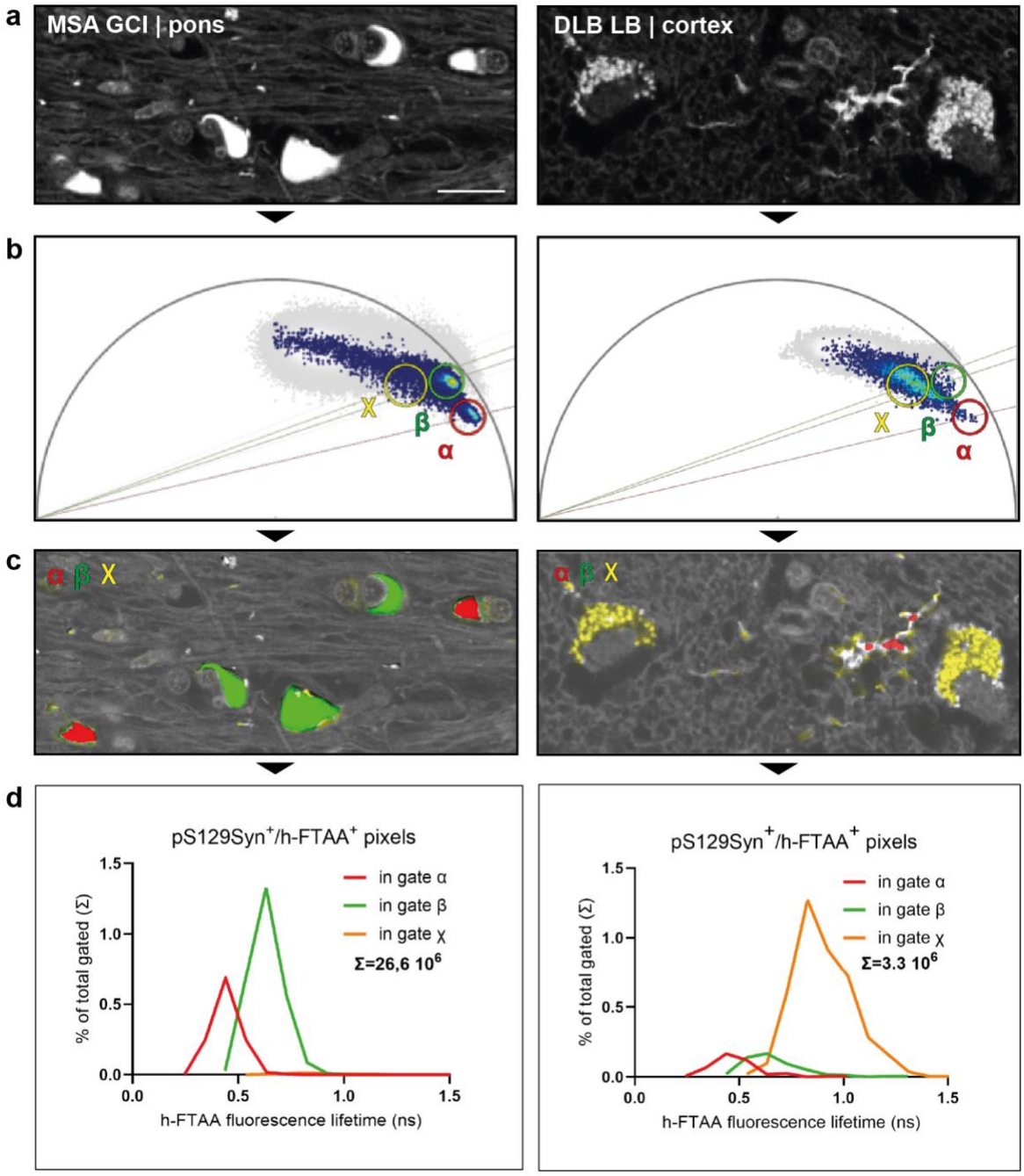

Extended Data Fig. 9 | h-FTAA is a conformation-sensitive probe that enables discrimination between aSyn fibril strains associated with MSA and DLB through FLIM of brain tissue sections. It was previously reported that FLIM of h-FTAA can be used in histological brain sections to differentiate the aSyn fibrils populating Lewy bodies (LBs) from those populating GCIs in MSA[37]. These findings established h-FTAA as a conformation-sensitive amyloid probe capable of discriminating distinct aSyn fibril strains in human brain sections via FLIM[37]. In agreement with these previous observations, FLIM of h-FTAA allowed us to derive fibril strain-specific phasor plot signatures directly on brain tissue sections. Using this approach, we confirmed that h-FTAA FLIM could indeed discriminate the pS129Syn-positive inclusion pathology of MSA vs. DLB (a: h-FTAA intensity images - pS129Syn not shown) and used the disease-specific hotspots in the respective FLIM phasor plots to define 2D quantification gates (**b,c**) (α, β: MSA-specific; χ: DLB-specific). The fluorescence lifetime of the gated pixels is shown in **d** for respectively GCIs (26,6 million inclusion pixels gated) and LBs (3.3 million inclusion pixels gated). In agreement with previously published

1042 data[37], the distribution histograms make it clear that the majority of pixels belonging to LBs are characterized
1043 by a fluorescence lifetime which is in the nanosecond range, while those populating GCIs show an
1044 approximately halved fluorescence lifetime with 2 distinguishable populations. Scale bar = 20 µm.

1045

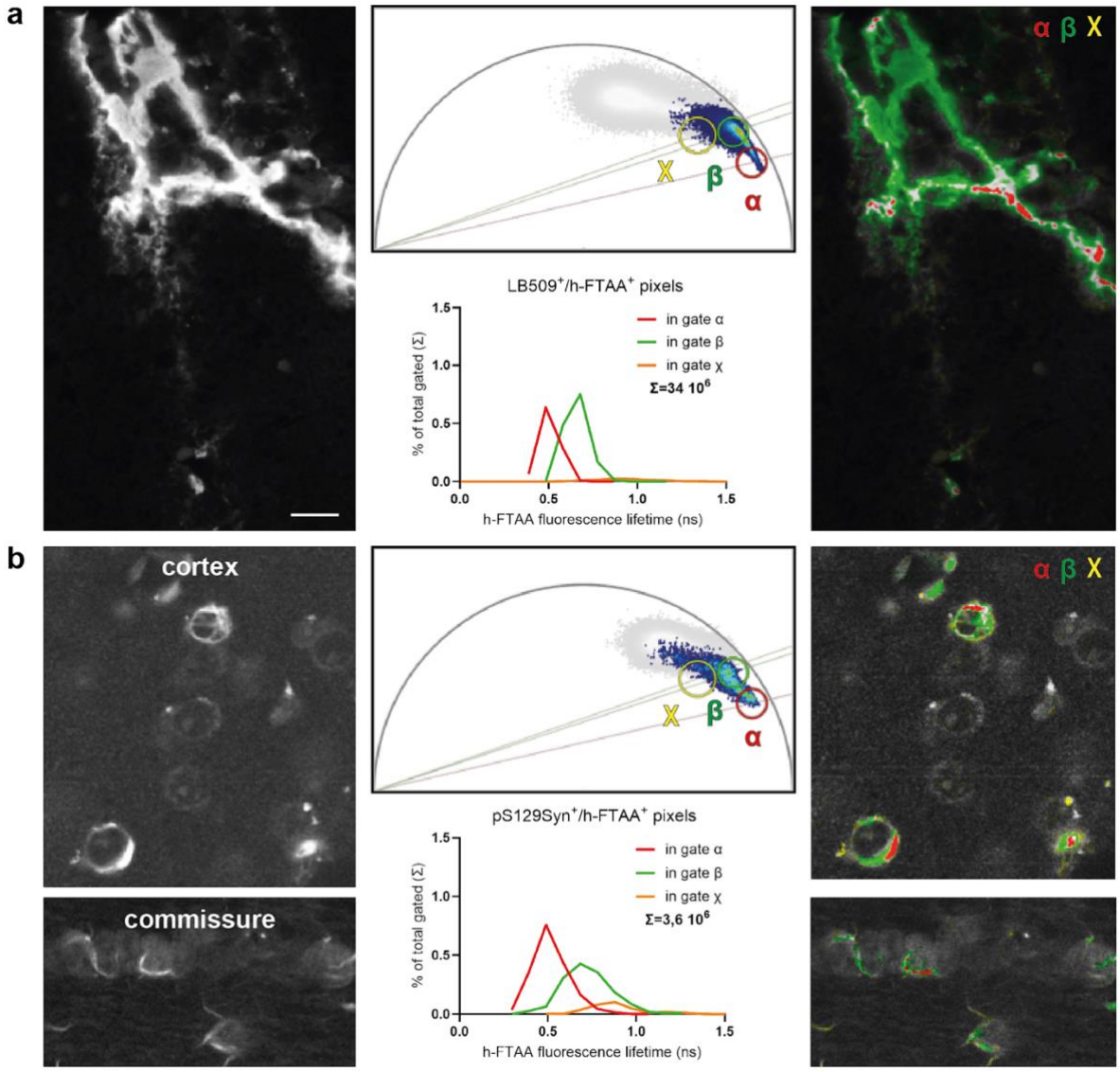

Extended Data Fig. 10 | *In situ* h-FTAA FLIM indicates that both the input 1B fibrils and the resulting inclusions seeded in wild-type mice exhibit a high degree of conformational similarity with the MSA strain. The phasor plot gates discriminating GCIs and LBs described in Extended Data Fig. 9 were applied in the phasor plots of the intracerebral 1B fibril inoculate (positive to the anti-human aSyn antibody LB509, not shown), still observable in the CP of wild-type mice 24 hours after injection (**a**, from left to right: h-FTAA intensity image, corresponding phasor plot with gates and quantifications, distribution of gated pixels in image) or in the plots characterizing the inclusions that formed in neurons and OLs during the 16 months following 1B injection (pS129Syn-positive, not shown) (**b**). The number of inclusion pixels quantified by FLIM and gated in α, β, and χ was $>10^6$ in each case, and the distribution of the pixel population in the phasor gates α+β, and χ was eventually used to score the similarity of the different fibril inclusion types (Table 3). Scale bar = 20 µm.

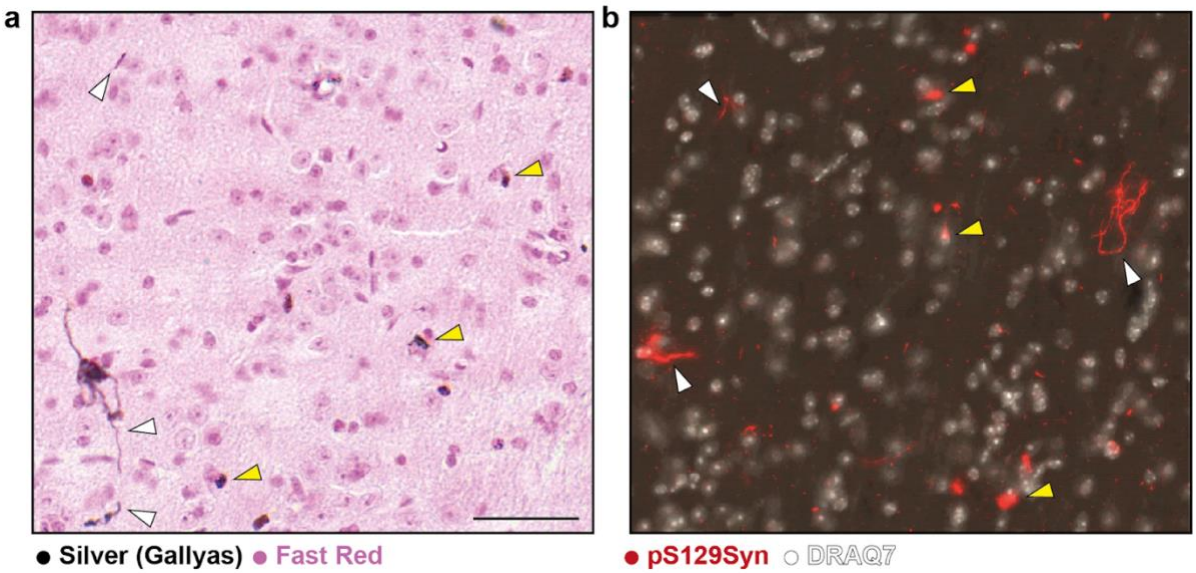

Extended Data Fig.11| The MSA-specific silver impregnation technique of Gallyas highlights somatic (yellow arrowheads) and neuritic (white arrowheads) inclusions which developed during 16 months in the substantia nigra of WT mice injected with 1B (**a**); other section in the same region reveals pS129Syn-positive inclusion pathology (**b**). Scale bar = 100 µm.

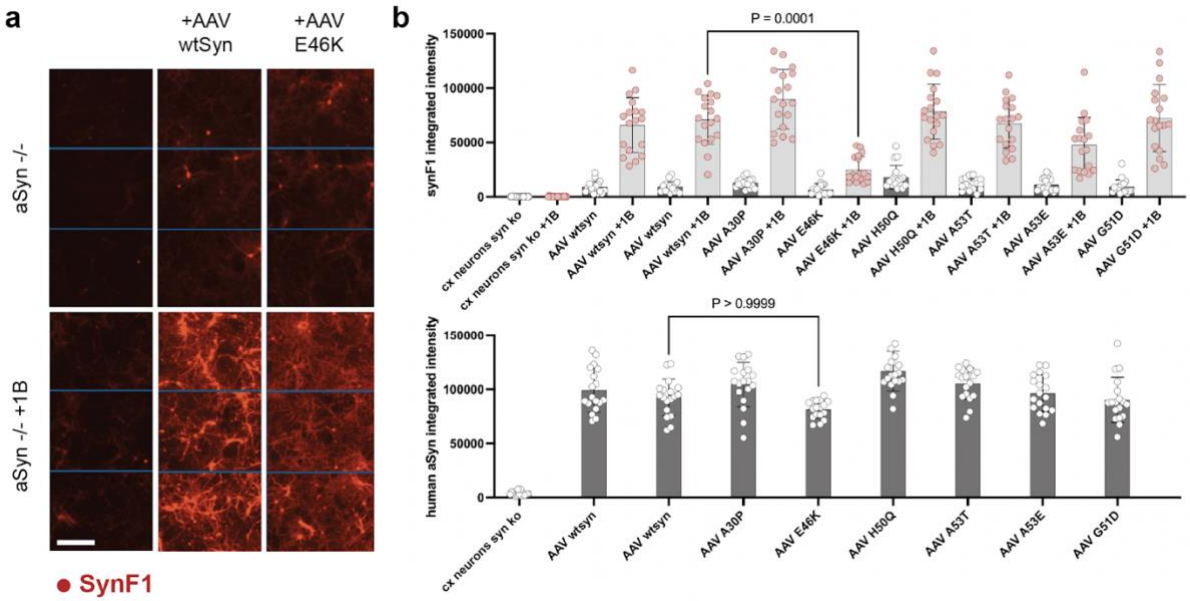

Extended Data Fig. 12 | Inclusion seeding by 1B is inhibited by E46K which disrupts the pseudo-Greek-key motif stem stabilizer (E46-K80 salt bridge), but not by aSyn mutations in the inter-protofilament interface. a. 96-well pooled primary cultures of cortical neurons from 8 aSyn-KO mouse embryos were challenged or not at day-in-vitro 7 (DIV7) with 10 nM 1B fibrils (equivalent aSyn monomer concentration), and infected or not with AAV-aSyn or AAV-E46K aSyn at DIV11. The neurons were fixed at DIV30 and the aSyn inclusions revealed using the conformation-dependent antibody SynF1 (red); three immunofluorescence fields of views (FOVs) imaged in a test well for each condition, illustrate: (i) the absence of SynF1and human aSyn signal at DIV30 in the absence of endogenous aSyn (aSyn-/- line, left column) , (ii) aSyn inclusion seeding by 1B in conditions of aSyn expression (aSyn -/- + 1B line, middle and right column), and (ii) a minor inclusion seeding when E46K aSyn is expressed instead of wild-type aSyn (aSyn -/- + 1B line, right versus middle column). **b.** High Content Analysis of the experiment shown in (a) and extended to a series of aSyn mutants based on 18 FOVs from 6 wells for each condition. The AAV-aSyn condition was doubled to document robustness. Kruskal-Wallis test followed by a post-hoc Dunn's test for multiple comparisons indicates that E46K aSyn is the only mutation reducing inclusion seeding by 1B (p= 0.0001). In the AAV-only conditions, human aSyn deriving from AAV infection was quantified using the human aSyn-specific antibody MJFR1 (no endogenous mouse aSyn is present in these neurons). The results were compared with the same test and post-hoc test combination as before, which indicated the absence of statistically significant differences in terms of levels of expression driven by the different AAVs. In particular, no statistically significant difference existed between AAV wt aSyn and AAV E46K aSyn in terms of expression levels, indicating that the difference seen with SynF1 after seeding with 1B was not due to a lesser expression of E46K aSyn. Scale bar = 100 µm.

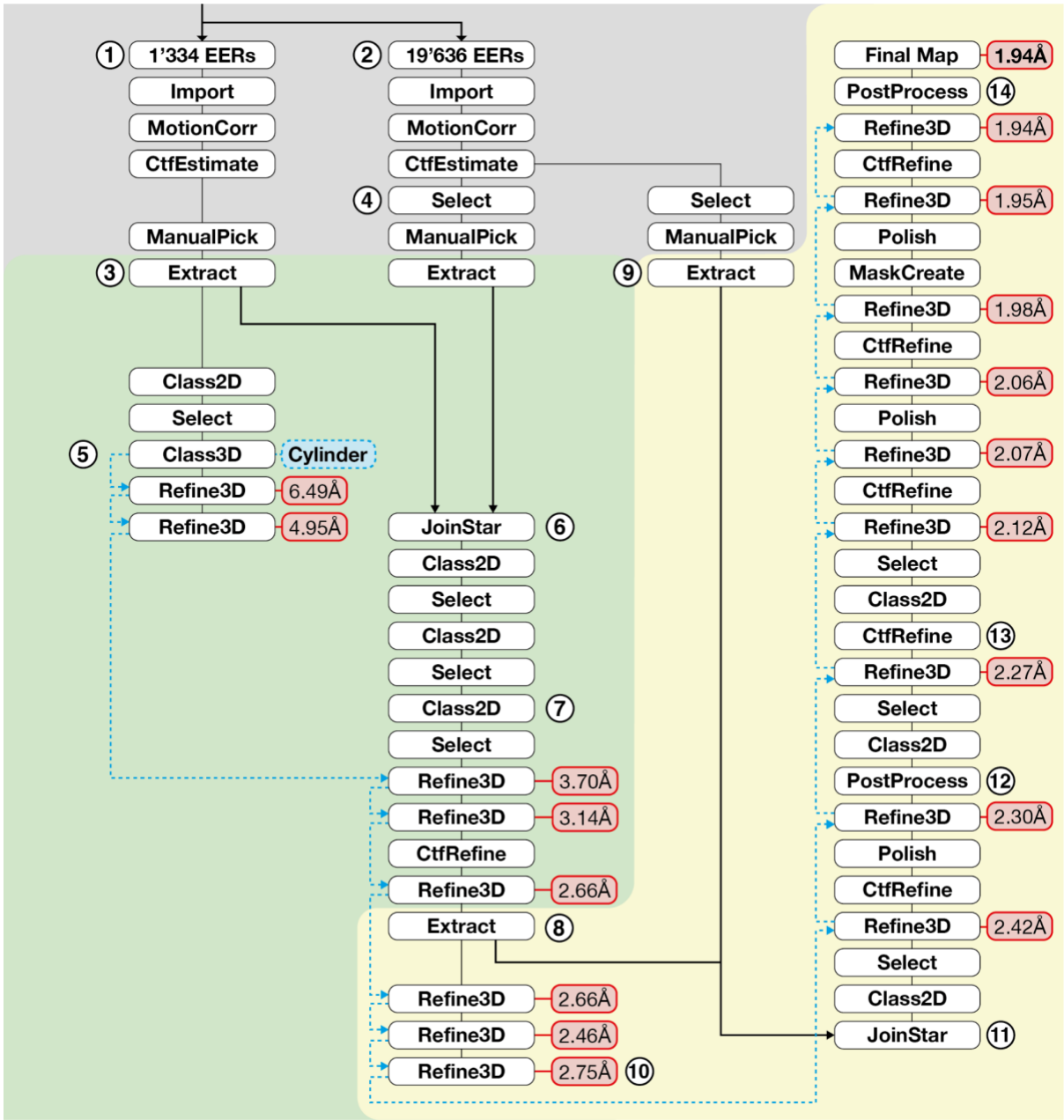

Extended Data Fig. 13 | Processing overview (schematic) for 1B reconstruction. Detailed processing overview representing individual jobs within RELION (white boxes), with the black line indicating subsequent steps. Red boxes indicate estimated resolution at given Refinement steps. Blue dotted line represents the reference volumes used. The background color represents data preprocessing (grey), binned processing (green), and unbinned processing (yellow). **1.** During data acquisition the first 1'334 micrographs (Electron Event Recordings) were processed during the session, to assess the quality of the dataset on the fly. **2.** The remaining 19'636 micrographs were processed after the data acquisition had completed and were later introduced to the dataset at step 6 and 11 respectively. **3.** For initial analysis manually traced fibril segments were extracted with a box size of 600px, binned to 300px. **4.** From the full dataset selections were made based on the estimated CTF resolution to reduce the amount of manual screening of the full dataset. As such two groups were analyzed: Add values. Manual picking of particles was done in parallel to the processing of the extracted particles from 3. **5.** Initial 3D-Classification was done with a featureless cylinder as a low-pass filtered reference volume. **6.** The first set of additional particles from the full data set was introduced to the processing. **7.** The full particle batch was cleaned by multiple rounds of 2D classification and was subsequently refined to 2.66Å with a reference volume from the previously obtained 4.95Å structure

from the initial screening. **8.** With a well-aligned structure, the data was transitioned to unbinned processing, and the respective particles were re-extracted. **9.** The second set of additional particles from the full dataset was extracted at the unbinned box size. No further manual selection of the full dataset was made. **10.** After transitioning to the unbinned box size the refinement was redone on the 2.66Å structure. **11.** All particles are joined together for the final processing. **12.** The structure was subjected to Refinement and PostProcessing with intermediate steps of Polish and **13.** CTF refinement until the final high-resolution structure was obtained. **14.** Processing concluded when no further improvement in the iterative process could be made. The model was built into the final map at 1.94Å resolution.

Supplementary information

Confocal animations/3D reconstructions:

Movie-1: Section hovering overview corresponding to **Fig. 1 panels a-e**: DAPI in blue, pS129Syn in white, Sox10 in pink, Iba1 in yellow (only in AC) Fig1a ACPL and BNST GCIs.mp4

Movie-2: 3D animation of NII & NCI shown in **Fig. 6 panel b, upper right**: DAPI in white, pS129Syn in green, Tyrosine Hydroxylase in red LeSTRIAP7 99c.mp4

Movie-3: 3D animation of NII shown in **Fig. 6 panel b, upper left**: DAPI in white, pS129Syn in green, Tyrosine Hydroxylase in red LeSTRIAP7 85.mp4

Movie-4: 3D animation of a Tyrosine Hydroxylase (red) positive cell from the s*ubstantia nigra* of the mouse sampled in **Fig. 6**. pS129Syn is in green. Both NCIs and NIIs can be observed without need for a nuclear marker LeSTRIAP7 97.mp4

Movie-5: 3D animation of **Fig. 6 panel b, lower left**: The NCI of the cortical neuron (bigger nucleus) seems to protrude within the interior of the lining glial cell (smaller nucleus): DAPI in white, pS129Syn in green, Tyrosine Hydroxylase in red (not expressed in this region) LeSTRIAP7 99a.mp4

Movie-6: "in silico" section of 3D animation of **Fig. 6 panel b, lower left**: The NCI is in continuity with a glial nuclear inclusion (GNI): DAPI in white, pS129Syn in green, Tyrosine Hydroxylase in red (not expressed in this region) LeSTRIAP7 99b.mp4

Tables

Table 1 | Structural comparison of different aSyn folds with 1B.

Structure comparison based on the RMSD value, as shown in **Fig. 3**. The fully modelled structures were aligned to the 1B conformation with the matchmaker function in ChimeraX. The best fit subunits were then further compared on three regions on the C-alpha RMSD values in respect to the different pocket regions and intermediate sequence based on ChimeraX RMSD measurements. RMSD below 1Å suggests high similarity in the structural conformation.

Structure PDB	Total Pairs Nr.	Total RMSD [Å]	N-Pocket RMSD (res. 39-47), [Å]	Intermediate RMSD (res. 48-87), [Å]	C-Pocket RMSD (res. 88-94), [Å]
H50Q Mutation 6PEO	61	0.566	0.504	0.547	0.693
MSA seeded 7NCK	61	0.781	0.597	0.815	0.892
1BP 9RZF	61	1.433	0.582	1.642	0.357
MSA purified 6XYQ	61	2.425	3.685	1.228	0.398
1-121 aSyn 6H6B	58	4.856	3.418	3.484	9.225
wt aSyn 8OQI	56	5.282	7.631	3.171	9.532
ThT bound 7YNM	61	4.688	4.643	3.225	8.511

1138 **Table 2 | Cryo-EM data collection, refinement, and validation statistics**

	1B fibril	**1B^P fibril**
Raw images	EMPIAR-12012	TBD
Reconstructed volume	EMD-19986	EMD-54402
Atomic model:	PDB-9EUU	PDB-9RZF
Data collection and processing		
Nominal Magnification	120’000x	165’000x
Voltage (kV)	300	300
Total electron dose (e/Å^2)	40	50
Defocus range (μm)	-0.8 to -1.8	-0.8 to -2.2
Pixel size (Å)	0.66	0.732
Symmetry imposed	C1 with 2_1 cork-screw symmetry	C1 with 2_1 cork-screw symmetry
Micrographs	11’879	42’812
Initial particle images (no.)	108’543	3’556
Final particle images (no.)	51’272	1’913
Map resolution (Å) FSC threshold at 0.143	1.94	3.8
Map resolution range (Å)	1.88-2.56	3.45-31.38
Estimated map sharpening B-factor (Å^2)	-21.06	-2.52
Helical twist (°)	179.52	179.55
Helical rise (Å)	2.43	2.40
Refinement		
Model resolution range (Å)	1.7 - 2.4	2.9 - 3.3
Model composition Non-hydrogen atoms Protein residues Ligands	 3400 496 0	 2538 366 0
B factor (Å^2) Protein	 21.06	 56.98
R.m.s. deviations Bond lengths (Å) Bond angles (°)	 0.001 0.490	 0.004 0.858
Validation MolProbity score Clashscore Poor rotamers (%)	 1.52 5.57 0.00	 1.83 7.84 0.00
Ramachandran plot Favored (%) Allowed (%) Disallowed (%)	 96.61 3.39 0.00	 94.07 5.93 0.00

1139

1140

Table 3 | *In situ* comparison of 1B inoculate, 1B-seeded inclusions, GCIs in MSA and LBs in DLB using h-FTAA FLIM of human and wild-type mouse brain tissue sections

Inclusion pixels quantified by FLIM and gated in α, β, and χ in **Extended data Fig. 10** (>10^6 in each case) were used for comparison of inoculate and inclusions. For each condition, the % of the inclusion pixel population situated in the phasor gates α+β (MSA specific), and χ (DLB specific) (see **Extended data Fig. 9),** was used to score the similarity of the different fibril inclusions types using the Jaccard similarity index[52]. Similarity matrix analysis demonstrates that both the input 1B fibrils and the resulting inclusions seeded in wild-type mice exhibit a high degree of conformational similarity which is shared with the MSA fibrils, and distinct from the DLB ones. Color coding: green = similar, yellow = dissimilar.

	MSA GCIs pS129Syn⁺	**1B-seeded** NCIs & GCIs pS129Syn⁺	**1B inoculate** LB509⁺	**DLB** LBs pS129Syn⁺
MSA GCIs pS129Syn⁺	1,000	0,900	0,762	0,160
1B-seeded NCIs & GCIs pS129Syn⁺	0,900	1,000	0,848	0,197
1B inoculate LB509⁺	0,762	0,848	1,000	0,259
DLB LBs pS129Syn⁺	0,160	0,197	0,259	1,000